



1 Assessment of satellite observation-based wildfire emissions inventories using

2 TROPOMI data and IFS-COMPO model simulations

3

4 Adrianus de Laat<sup>1,#</sup>

5 Vincent Huijnen<sup>1</sup>

6 Niels Andela<sup>2</sup>

7 Matthias Forkel<sup>3</sup>

8

9 # corresponding author, [laatdej@knmi.nl](mailto:laatdej@knmi.nl)

10 <sup>1</sup>Royal Netherlands Meteorological Institute, de Bilt, the Netherlands

11 <sup>2</sup>BeZero Carbon, London, United Kingdom

12 <sup>3</sup>Technical University Dresden, Germany



13 **Abstract**

14 Fires are a key component of the global carbon cycle and humans are changing their  
15 characteristics. Fire emission monitoring is important to keep track of those changes and  
16 TROPOMI satellite observations of tropospheric nitrogen dioxide, carbon monoxide and the  
17 absorbing aerosol index can be used to quantify and verify the accuracy and precision of global  
18 wildfire emission estimates on a daily basis. Here we use TROPOMI observations to evaluate  
19 a new fire emission database based on Global Fire Atlas input for the Sense4Fire project (GFA-  
20 S4F) and from the Copernicus Atmosphere Monitoring (CAMS) Global Fire Assimilation  
21 System (GFAS) for a number of test regions worldwide representative of the most important  
22 wildfire type environments. The main focus is on Amazon and Cerrado biomes (tropical rain  
23 forests and deforestation) during August-September 2020, but analyses are also made for a  
24 region in sub-Saharan Africa (savannah) as well as two regions in Siberia (steppe and boreal  
25 forests/tundra). GFA-S4F and GFAS fire emissions are used as input for global atmospheric  
26 composition model simulations based on IFS-COMPO, *i.e.* an extension of ECMWF's  
27 Integrated Forecasting System (IFS) for simulating atmospheric composition. Comparing the  
28 model output with the TROPOMI observations then provides an indirect check on the realism  
29 of these emission estimates. Furthermore, for tropospheric nitrogen dioxide the IFS-COMPO  
30 model simulations are also used to estimate the model sensitivity of tropospheric nitrogen  
31 dioxide columns with respect to fire emission changes. This local relationship is used to  
32 optimize the fire NO<sub>x</sub> emissions directly using the TROPOMI nitrogen dioxide observations.

33 The results reveal that for small fires emission nitrogen dioxide estimates are realistic on  
34 average albeit with a large spread, *i.e.* for individual fires emissions can be significantly under  
35 or overestimated regardless of emission database. However, for large fires nitrogen dioxide  
36 emissions are systematically and largely overestimated in all four regions. The overestimation  
37 can be an order of magnitude or even more. For area total nitrogen dioxide emissions this "large



38 fire bias” is of minor importance, *i.e.* total nitrogen dioxide emissions are dominated by small  
39 fires. The GFA-S4F emission estimates were characterized by a larger positive bias for large  
40 fire NO<sub>2</sub> emission cases compared to GFAS. The source of this bias is not well understood.  
41 With optimized NO<sub>2</sub> emissions by direct adjustment of emission using TROPOMI nitrogen  
42 dioxide observations the large positive bias can efficiently be resolved. Combined with an  
43 update of soil NO<sub>x</sub> emissions – causing too low background NO<sub>x</sub> levels – a fairly good  
44 agreement between IFS-COMPO and TROPOMI was reached.

45 Carbon monoxide was generally underestimated using GFAS emission (~50% on average  
46 for the selected regions). Updating carbon monoxide emissions over the Amazon region by  
47 incorporating more Sentinel satellite data (GFA-S4F) did reduce this fire CO bias significantly  
48 (to ~25% on average).

49 Overall, the results show that TROPOMI data allows for systematically identifying  
50 uncertainties and errors in satellite-data based fire emissions. The results also suggest that the  
51 use of dynamic emission factors may further improve satellite based global emissions  
52 inventories. In addition, the results also highlight that the use of TROPOMI data could be much  
53 more detailed and refined towards assessing individual fires on a daily basis for better  
54 understanding fire dynamics and to improve and diversify fire emission factors.



55 **1. Introduction**

56 Disturbance of vegetation by fire - anthropogenic or natural - is a major contributor to the  
57 amount of carbon (as carbon dioxide or methane) present in the atmosphere (Lasslop et al.,  
58 2019; Bowman et al., 2020; McLauchan et al., 2020). Vegetations fires are also important for  
59 the natural cycle of vegetation growth in many parts of the world and burning vegetation is a  
60 practice also used by humans in farming. The associated time scales can vary from several  
61 weeks to hundreds of years depending on vegetation type and speed of regrowth. Wildfire  
62 extremes and associated smoke can be disrupting to livelihoods as for example in Australia  
63 2019 (Boer et al., 2020; Filkov et al., 2020) or the US West Coast 2020 (Higuera and  
64 Abatzoglou, 2021).

65 Satellite sensors can provide a number of key pieces of information to characterize  
66 vegetation fires (Chuvienco et al., 2019, 2020; Wooster et al., 2021). These include detection of  
67 thermal anomalies indicative of active fires, the energy released (fire radiative power or FRP),  
68 the loss of vegetation expressed as a change in surface reflectance indicative of burnt area and  
69 fire severity, or biomass loss, and observations of aerosols or atmospheric trace gases directly  
70 associated to, and traceable back to, fire events. Each individual dataset contains valuable fire  
71 information in itself but a greater understanding of the role of vegetation fires globally can be  
72 obtained by combining these datasets into one information system. Although several satellite-  
73 derived fire emission databases exist, there continues to be a need to develop additional  
74 validation methodologies and data products to advance our understanding of satellite-derived  
75 estimates of individual fire behavior (Andela et al., 2019, 2022; Andreae, 2019).

76 Earth observation can also help in constraining fire emission estimates. In particular carbon  
77 monoxide (CO) has been used for evaluation of fire emission estimates with various  
78 techniques, including formal emission inversions (Hooghiemstra et al., 2011; Yin et al., 2015),



79 mass budget analyses (Huijnen et al., 2016), Gaussian plume modelling (Adams et al., 2019)  
80 as well as estimating fire CO<sub>2</sub> emissions using carbon monoxide as a proxy (Peiro et al., 2022).  
81 Likewise aerosol and formaldehyde (HCHO) observations have been used as fire emission  
82 proxies (Petrenko et al., 2012; Konovalov et al., 2014; Stavrakou et al., 2015; Bauwens et al.,  
83 2016). However, in any of these methods the estimated carbon emissions are subject to  
84 uncertainties in bottom-up emission estimates due to emission factors, the dynamics of the  
85 emission process in the atmosphere and tracer lifetime. Limitations to data quality and the  
86 spatio-temporal coverage of satellites further hamper in depth analysis of fire emissions to  
87 larger regional to continental scales for many studies and trace gases (Alvarado et al., 2011;  
88 Mebust et al., 2011, 2013, 2014; Young and Paton-Walsh, 2011; Castellanos et al., 2014;  
89 Schreier et al., 2014; Tanimoto et al., 2015; Whitburn et al., 2015; Sitnov and Mokhov, 2017;  
90 Lee et al., 2019; Adams et al., 2019; Lin et al., 2020).

91 The launch of the TROPOMI instrument on board of Polar orbiting Sentinel-5p satellite in  
92 October 2017, with at that time unprecedented spatial resolution, data accuracy and precision,  
93 has opened up a whole new range of possibilities for monitoring and studying fires. Several  
94 research papers have been published in recent years exploring the use of TROPOMI CO and  
95 NO<sub>2</sub> often in conjunction with FRP data from other satellites (Li et al., 2020; Griffin et al.,  
96 2021; 2023; Jin et al., 2021; van der Velde et al., 2021; Stockwell et al., 2022; Wan et al., 2023;  
97 see the Appendix for a brief summary of all these papers). These studies highlight the potential  
98 of using TROPOMI data for assessing fire emissions. However, they also all note that their  
99 studies are only first exploratory steps using TROPOMI and that more research is needed and  
100 warranted while approaches could be expanded, extended and refined.

101 The ESA Sense4Fire project (S4F) explores the suite of the Sentinel satellite instruments  
102 using a novel synergetic approach to derived global fire emissions based on the characterization



103 of individual fires and their behavior, eventually to better constrain total carbon emissions and  
104 emission factors. Atmospheric chemical composition modelling is used as an interface between  
105 Sentinel 2 and sentinel 3 based emissions vs. TROPOMI observations.

106 The objective of this study is to evaluate daily emission estimates of NO<sub>2</sub> and CO from the  
107 Global Fire Atlas (GFA-S4F) and the Global Fire Assimilation System (GFAS) by using them  
108 as input for atmospheric chemistry model simulations. The model results are compared with  
109 TROPOMI observations of NO<sub>2</sub> and CO to assess the realism of these emission estimates. The  
110 method described above is an indirect validation method in which the atmospheric composition  
111 modelling results act as interface between the emission estimates and the TROPOMI data. We  
112 therefore also apply an innovative approach for further updating and improving the emission  
113 estimates that makes more direct use of TROPOMI observations.

## 114 **2 Data and methods**

### 115 **2.1 TROPOMI data**

116 The Sentinel-5 precursor satellite, launched on 13 Oct. 2017 in an ascending sun-  
117 synchronous polar orbit, with an equator crossing at about 13:30 local time, carries the  
118 TROPospheric Monitoring Instrument (TROPOMI; Veefkind et al., 2012). Sentinel-5p is one  
119 of the Sentinel satellites of the European Copernicus Program dedicated to monitoring  
120 atmospheric composition. TROPOMI is a spectrometer that provides measurements in four  
121 channels – ultraviolet (UV), visible (VIS), near infrared (NIR) and shortwave infrared (SWIR)  
122 - of several atmospheric trace gases including NO<sub>2</sub> and CO and of cloud and aerosol  
123 properties. The TROPOMI instrument is unique in several ways because it combines near-daily  
124 global coverage with a wide spectral range, UV/VIS/NIR foot prints of 3.5×5.5 km<sup>2</sup> at nadir



125 (3.5×7 km<sup>2</sup> before 6 August 2019), SWIR footprints of 5.5×7 km<sup>2</sup> at nadir (7×7 km<sup>2</sup> before 6  
126 August 2019) and a very large signal-to-noise ratio.

### 127 **2.1.1 Tropospheric nitrogen dioxide (NO<sub>2</sub>)**

128 In this paper we use the TROPOMI NO<sub>2</sub> offline data from data processor version 2.3.1 and  
129 algorithm version 1.5.0. The operational TROPOMI NO<sub>2</sub> product is described in van Geffen et  
130 al. (2020). Detailed information can be found in the Product README File (PRF; Eskes and  
131 Eichmann, 2021), the Product User Manual (PUM; Eskes et al., 2022) and the Algorithm  
132 Theoretical Basis Document (ATBD; van Geffen et al., 2021).

133 Validation of TROPOMI tropospheric NO<sub>2</sub> columns for the biomass burning regions that  
134 S4F focuses on is missing due lack of ground-based stations in those areas. The general  
135 validation results for comparison with ground-based data (Verhoelst et al., 2021; Lambert et  
136 al., 2023) indicate a negative bias for the tropospheric column data with a median value of 28%  
137 with a range of 13% for rather clean locations to 40% over extremely polluted sites. The largest  
138 differences occur during winter at higher latitudes (van Geffen et al., 2022). Note that these  
139 biases fall (well) within the mission requirement of less than 50% bias. On the other hand,  
140 given the lack of validation sites in the areas of interest of this paper – and in particular in the  
141 tropical rain forest Amazon region and the south-of-the-equator African Savannah region it is  
142 unclear how large TROPOMI tropospheric NO<sub>2</sub> columns biases are in those regions and  
143 whether the validation would improve with the updated algorithm.

### 144 **2.1.2 Carbon Monoxide (CO)**

145 The TROPOMI CO total column retrieval algorithm derives data in the 2315–2338 nm  
146 spectral range of the SWIR part of the solar spectrum and retrieves the CO values for clear-sky  
147 conditions over land and low clouds over the ocean (Borsdorff et al., 2014; Landgraf et al.,



148 2016; Schneising et al., 2019). TROPOMI CO measurements are sensitive to the integrated  
149 amount of CO along the light path, including the contribution of the planetary boundary layer,  
150 making them particularly suitable for detecting surface sources of CO.

151 The operational TROPOMI CO retrieval deploys a profile scaling approach where a CO  
152 reference profile is scaled to fit the TROPOMI reflectance measurements. For this, global,  
153 monthly averaged vertical CO *a priori* profiles are used from the chemical transport model  
154 TM5 (Krol et al., 2005). The forward calculation of the TROPOMI spectral measurements  
155 account for light scattering by clouds and aerosols in the atmosphere and thus simultaneously  
156 retrieves trace gas columns and effective parameters describing the cloud contamination of the  
157 measurements (height scattering layer, scattering optical thickness) as demonstrated by Vidot  
158 et al. (2012).

159 In this paper we use the TROPOMI CO offline data from data processor version 1.3.2 and  
160 algorithm version 1.2.0. As recommended in the TROPOMI README file (Landgraf et al.,  
161 2022a) and the product user manual (PUM; Apituley et al., 2022), we only use data with quality  
162 assurance values (qa\_values) larger than 0.5. More details about the algorithm can be found in  
163 the Algorithm Theoretical Basis Document (ATBD; Landgraf et al., 2022b) that provides a  
164 detailed reanalysis description of the implementation of the CO retrieval.

165 TROPOMI CO validation papers consistently report only small and mostly random biases  
166 up to an order of magnitude smaller than the standard deviation of differences when compared  
167 to ground-based observations, data and other satellite data. Correlations are generally high, and  
168 biases are generally in the order of a few percent or less (Borsdorff et al., 2018, Martínez-  
169 Alonso et al., 2020; Sha et al., 2021; Lambert et al., 2023). The differences fall well within the  
170 TROPOMI mission requirements on accuracy (<15 %) and precision (<10 %) in CO total  
171 columns. The data does suffer from striping issues and instrument effects in the area of the





172 South Atlantic Anomaly (SAA). For CO there is one validation site in the S4F Amazon area of  
173 interest: Porto Velho. Validation results for Porto Velho reveal an excellent correlation (0.96)  
174 and small bias (0.51%) in total CO columns of the offline data product (Lambert et al., 2023).

### 175 **2.1.3 Absorbing Aerosol Index (AAI)**

176 The AAI is a well-established satellite data product that has been produced for several  
177 different satellite instruments spanning a period of more than 30 years. The AAI was first  
178 calculated as a correction for the presence of aerosols in column ozone measurements made by  
179 the TOMS instruments (Herman et al., 1997; Torres et al., 1998) because it was observed that  
180 ozone values were too high in typical regions of aerosol emission and transport. The AAI is  
181 based on spectral contrast in the ultraviolet spectral range for a given wavelength pair, where  
182 the difference between the observed reflectance and the modeled clear-sky reflectance results  
183 in a residual value. When this residual is positive, it indicates the presence of UV-absorbing  
184 aerosols, like dust, smoke, or volcanic ash. Clouds yield near-zero residual values, and negative  
185 residual values can be indicative of the presence of non-absorbing aerosols (*e.g.*, sulfate), as  
186 shown by sensitivity studies of the AAI (de Graaf et al., 2005; Penning de Vries et al., 2009).  
187 Unlike satellite-based aerosol optical thickness measurements, the AAI can also be calculated  
188 in the presence of clouds so that daily global coverage is possible. This is ideal for tracking the  
189 evolution of episodic aerosol plumes from dust outbreaks, volcanic eruptions, and biomass  
190 burning. For this study, we use the TROPOMI AAI data for the wavelength pair 340–380 nm.  
191 For more details about the TROPOMI AAI retrieval algorithm, see Stein-Zweers (2016). In  
192 this paper we use the TROPOMI AAI offline data from data processor version 1.3.2 and  
193 algorithm version 1.2.0.

## 194 **2.2 Methods**



195 We use fire emission data from two emissions inventories based on satellite data: the Global  
196 Fire Atlas (GFA; Andela et al., 2017, 2019, 2022) emissions and the Global Fire Assimilation  
197 System emissions (GFAS; Kaiser et al., 2012). We further use IFS-COMPO atmospheric  
198 chemistry and transport model simulations (Huijnen et al., 2019; Williams et al., 2022),  
199 TROPOMI data (Veefkind et al., 2012), and the innovative  $\beta$ -method for updating emissions  
200 based on TROPOMI data (Lamsal et al., 2011; Castellanos et al., 2014). We also perform a  
201 number of IFS-COMPO model experiments varying emissions or model processes/parameters  
202 in order to better understand differences we find between IFS-COMPO and TROPOMI. The  
203 particular experiments will be described in more detail later on (Table 2).

204 We perform an analysis in four study regions (see Appendix Fig. A1 and later Table 2) that  
205 show a large variation of biomes and fire types. The main focus of this study is the  
206 Amazon/Cerrado region; other regions are south-equatorial Africa savannahs, north Siberian  
207 boreal forests and tundra, and central Siberian steppes. For the S4F project four  $5^\circ \times 5^\circ$  areas  
208 were selected to limit the high computation demand for calculating satellite data-based  
209 emissions. However, given the IFS-COMPO resolution of  $0.5^\circ$ , a daily  $5^\circ \times 5^\circ$  area would  
210 frequently yield too little data for meaningful statistics. Hence why for this study we expanded  
211 the coverage of the four regions (see later Table 2) to derive sufficient daily comparison data  
212 of IFS-COMPO with TROPOMI data for meaningful statistics. Note that for the  
213 Amazon/Cerrado we will refer to both the smaller and larger region, also to accommodate  
214 future S4F research and publications.

### 215 **2.2.1 Global Fire Atlas - based emissions**

216 The Global Fire Atlas approach tracks individual fire events-based Moderate Resolution  
217 Imaging Spectroradiometer (MODIS) burned area (Andela et al., 2019) or Visible Infrared  
218 Imaging Radiometer Suite (VIIRS) active fire data (Andela et al., 2022). The VIIRS-based



219 method was developed to fill the need for a near-real-time approach for tracking contributions  
220 from deforestation, forest, agricultural, and savanna fires to burned area and carbon emissions.  
221 The approach was applied to the Amazon and Cerrado region, defined as the area 25°S-EQ,  
222 85°W-30°W, for the years 2019 and 2020 although here we only will focus on emissions for  
223 August and September 2020. Here we apply emissions factors derived from Andreae et al.  
224 (2019) to translate carbon emissions to NO<sub>x</sub> and CO emissions for each fire type. The following  
225 emissions factors (grams trace gas per kg matter burned) were used for grasslands and savanna  
226 fires (69.2 and 2.49 g kg<sup>-1</sup>), small clearing and agricultural fires (102 and 3.11 g kg<sup>-1</sup>), forest  
227 fires (98 and 1.94 g kg<sup>-1</sup>), and deforestation fires (99 and 4.63 g kg<sup>-1</sup>) for NO<sub>x</sub> (as NO) and CO,  
228 respectively.

### 229 **2.2.2 GFAS fire emissions**

230 The Global Fire Assimilation System (GFAS; Kaiser et al., 2012) estimates dry matter  
231 combustion rates by multiplying FRP and biome-specific emission factors. The global  
232 distribution of FRP observations is obtained from the MODIS instruments on board the Terra  
233 and Aqua satellites and are then assimilated into the GFAS system. The gaps in FRP  
234 observations, which are mostly due to cloud cover and spurious FRP observations of volcanoes,  
235 gas flares, and other industrial activity, are corrected or filtered in the GFAS system. Eight  
236 biome-specific emission factors are used based on linear regressions between the GFAS FRP  
237 and the dry matter combustion rate of Global Fire Emission Database (GFED) version 3.1 in  
238 each biome (see later Table 2 and Fig. 3 in Kaiser et al. (2012)). The biomass burning emission  
239 of a given species is then calculated by multiplying the dry matter combustion rate with an  
240 emission factor of that species.

### 241 **2.2.3 IFS-COMPO**



242 As outlined in the introduction this study uses an atmospheric chemical composition model  
243 (IFS-COMPO, previously known as "C-IFS" (Flemming et al., 2015)) as an interface between  
244 Sentinel 2 and sentinel 3 based emissions and TROPOMI observations. IFS-COMPO is an  
245 extended version of ECMWF's Integrated Forecasting System that was developed as part of  
246 the global component of CAMS which includes modeling and assimilation of atmospheric  
247 composition (aerosols, trace gases and greenhouse gases). Here we use a version of IFS-  
248 COMPO which is set to simulate tropospheric chemistry and aerosol but excluding data  
249 assimilation of atmospheric composition (see Appendix).

250 IFS-COMPO is run at a horizontal resolution of T511 (approximately 40 km grid cell), with  
251 137 vertical levels and a time step of 900s. This default configuration of IFS-COMPO uses  
252 CAMS-GLOB-ANT v5.3 anthropogenic emissions (Soulie et al., 2023), together with CAMS-  
253 GLOB-BIO v3.1 biogenic emissions, and soil NO<sub>x</sub> emissions based on POET. The GFASv1.4  
254 emissions, with updated emission factors for CO and NO, are applied globally. A series of  
255 sensitivity experiments have been conducted, primarily testing the sensitivity in the fire input  
256 emissions (Tables 1 and 2). To compare TROPOMI observations with IFS-COMPO output we  
257 take into account all relevant aspects that are required when matching observation data to  
258 model data including averaging kernels. Only TROPOMI observations with quality assurance  
259 threshold above 0.75 are used, as recommended by the NO<sub>2</sub> product user manual. This concerns  
260 observations with cloud radiance fraction of less than 0.5 and excludes retrievals with ground  
261 pixels covered with snow/ice, as well as problematic retrievals.

262 The model fields are interpolated in time to match with local overpass time of TROPOMI  
263 and the averaging kernel is applied to the model NO<sub>2</sub> profile. The collocated model-observation  
264 pairs are gridded on a common 0.5°×0.5° output field (or different resolution, which is  
265 configuration setting), and only written to output files if a threshold coverage of 50% of the



266 grid cell is reached. The averaging is done by an area-weighted approach, hence taking into  
267 account the area of the TROPOMI-pixel that is within the model grid box (Douros et al., 2023).

268        Similar to the evaluation of IFS-COMPO NO<sub>2</sub>, we use TROPOMI observations of CO total  
269 columns to evaluate model CO columns, selecting observations with quality assurance  
270 threshold above 0.5. The model total column fields are interpolated in time to match with local  
271 overpass time of TROPOMI. The same grid for collocation is used as was adopted for the  
272 evaluation against TROPOMI NO<sub>2</sub>, again only grid cells with a threshold coverage of 50% are  
273 used. Also the area averaging is the same as done for NO<sub>2</sub>.

274        Because the TROPOMI CO column data is nearly uniformly sensitive to height (Borsdorff  
275 et al., 2014) we will assume for comparison with IFS-COMPO that TROPOMI CO column  
276 data represents a true vertical column so that no weighting or sensitivity correction on IFS-  
277 COMPO CO data needs to be applied.

#### 278 **2.2.4 $\beta$ -method**

279        The basic approach followed in this paper is to use the IFS-COMPO model as  
280 “intermediate” between the fire emission databases based on GFA or the GFAS emissions  
281 database on the one end and the TROPOMI observations on the other end.

282        The IFS-COMPO model, however, also allows for applying a different approach to use  
283 TROPOMI observations to modify and update model emissions by using the model simulations  
284 to derive the local relationship between emissions and satellite measurements (Lamsal et al.,  
285 2011; Castellanos et al., 2014). Although models like IFS-COMPO may simulate incorrect  
286 trace gas amounts due to errors in fire emission estimates, they are capable of realistically  
287 simulating changes in column amounts caused by changes in emissions. By performing a  
288 baseline model simulation and a “perturbed emission” simulation, a local column-emission



289 sensitivity parameter  $\beta$  can be derived as function of space and time that connects changes in  
290 column amounts ( $\Delta\text{TCNO}_2$ ) to changes in emissions ( $\Delta E$ ):

291 
$$\frac{\Delta E}{E} = \beta \frac{\Delta\text{TCNO}_2}{\text{TCNO}_2}$$

292 Then, differences in measured and modelled columns can be converted into differences in  
293 emissions relative to the baseline emissions by multiplication with the  $\beta$  parameter yielding an  
294 updated TROPOMI-based emission estimate. Here, we use the  $\beta$ -method to assess to what  
295 extent the prior fire NO<sub>x</sub> emission databases can be updated with this method to close the gap  
296 between model simulations of fire NO<sub>x</sub> emission plumes and TROPOMI observations of NO<sub>2</sub>.  
297 For this we run sensitivity experiments where we scale down the prior fire emissions (either  
298 GFAS or GFA-S4F) by 20%, and use the resulting change in tropospheric NO<sub>2</sub> columns to  
299 compute local and daily varying  $\beta$  values.

300 The  $\beta$  value is determined by local atmospheric chemistry conditions and background NO<sub>x</sub>  
301 emissions in IFS-COMPO. A  $\beta$  value of one (1.0) indicates that the relative change in emissions  
302 corresponds with a similar relative change in tropospheric NO<sub>2</sub> columns.  $\beta$  values < 1.0  
303 indicating relatively low sensitivity of fire emission changes to column changes ( $\beta$  values > 1.0  
304 indicative of the opposite). Very small  $\beta$ -values indicate limited sensitivity of emissions to  
305 changes in column values, very large  $\beta$ -values indicate high sensitivity of emissions to small  
306 changes in column values. Hence why  $\beta$ -values close to 1.0 are preferred and why we also limit  
307  $\beta$ -values to the 0.25-4.0 range.

308 To ensure that the  $\beta$  field only relate to fire emissions we additionally apply a filtering  
309 procedure to exclude instantaneous values of  $\beta$  when prior emissions are smaller than 0.1 mg  
310 m<sup>-2</sup> d<sup>-1</sup> and model NO<sub>2</sub> columns are smaller than  $2 \times 10^{15}$  molecules cm<sup>-2</sup>, and additionally take



311 the local median value of  $\beta$  computed based a two-month time series (August-September 2020).  
312 Over the Amazon, more than 97% of the median  $\beta$  values fall within the 0.5-2.0 range with  
313 60% within the 1.0-1.5 range (see Appendix Fig. A2). Note that on average  $\beta$ -values get closer  
314 to 1.0 for larger tropospheric  $\text{NO}_2$  column values indicating that the larger emissions, the more  
315 linear and straightforward the relation between emissions and  $\text{NO}_2$  column values.

316 Applying the  $\beta$ -method comes with a number of caveats and limitations. It does require  
317 prior emissions to be present for a given grid location in the IFS-COMPO model if the  
318 emissions are to be updated. This is a different approach from for example emission inversion  
319 methods that do not require any *a priori* information (Mijling et al., 2013; Ding et al., 2017).  
320 Also, given the differences in spatial resolution between IFS-COMPO, TROPOMI data and  
321 the emission databases need to be kept in mind. The  $\beta$ -method only allows to translate  
322 TROPOMI column enhancements into emission optimization within the (coarser) model grid  
323 resolution, which is valid for trace gases with sufficiently short lifetime such as  $\text{NO}_2$ .  
324 Furthermore, the  $\beta$ -method assumes that column amounts and emissions vary linearly which  
325 may not always be the case. Hence why  $\beta$  values close to a value of 1.0 are preferred and large  
326 changes in emissions far beyond the 20% model emission perturbation should be carefully  
327 considered. In principle non-linear relationships between column amounts and emissions could  
328 be overcome by applying the method iteratively albeit at the cost of requiring more model  
329 simulations and thus time. Nevertheless, once the model simulations have been performed the  
330  $\beta$ -method provides a straightforward method to use TROPOMI data for a rapid first order  
331 update of *prior* emissions.

### 332 **3. Results**

#### 333 **3.1 Amazon**

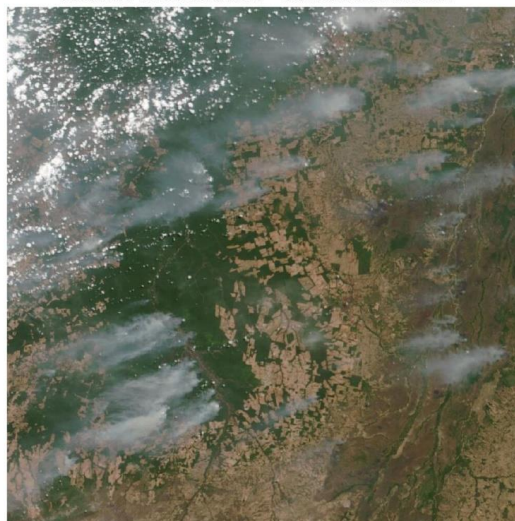


334 Fig. 1 show a SUOMI-NPP VIIRS image for 11 September 2020 over the selected  
335 Sense4Fire Amazon region as well as the larger Amazon region. They reveal a pattern typical  
336 for this Amazon region during this time of the year. There are widespread fires and smoke  
337 plumes visible over regions where deforestation is taking place. There is some shallow  
338 convection present, but weather conditions are mainly dry. Smoke from the fires covers a large  
339 region in the Amazon (Fig. 1, lower panel), resulting in accumulation of pollution with the  
340 Andes mountains to the west acting as a barrier for transport of pollution out of the region.





SUOMI-NPP VIIRS RGB 20200911 source © NASA EARTHDATA



(a)

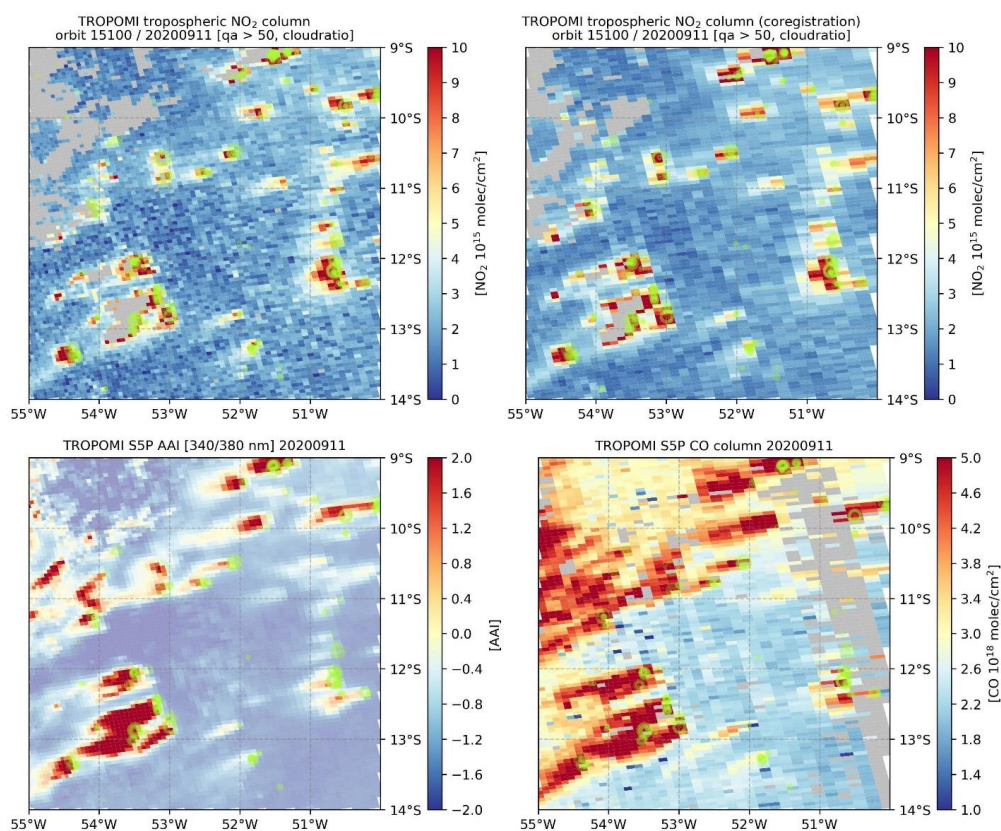
SUOMI-NPP VIIRS RGB 20200911 source © NASA EARTHDATA



(b)

341

342 **Figure 1.** (a) SUOMI-NPP VIIRS RGB image on 11 September 2020 over the Amazon region  
343 between  $50^{\circ}\text{W}$ - $55^{\circ}\text{W}$ ,  $9^{\circ}\text{S}$ - $14^{\circ}\text{S}$ . Image obtained from NASA WorldView based on the python  
344 script by Brian Blaylock (Univ. Utah, 2015); (b) as Fig. 1a but for  $50^{\circ}\text{W}$ - $70^{\circ}\text{W}$ ,  $5^{\circ}\text{S}$ - $25^{\circ}\text{S}$ . The  
345 area of Fig. 1a is denoted by the white square.



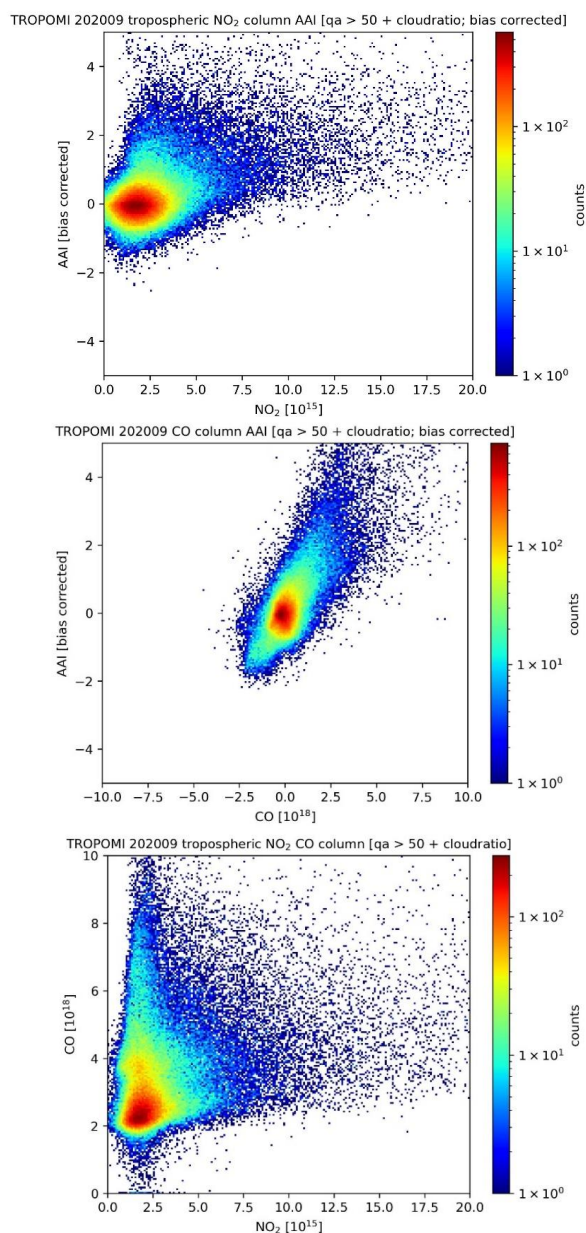
346

347 **Figure 2.** TROPOMI measurements of tropospheric NO<sub>2</sub> column (original resolution a  
 348 regridded to the CO grid), the CO total column and the AAI on 11 September 2020 for the  
 349 region shown in Fig. 1 (upper panel). The open green circles depict coincident NPP-VIIRS  
 350 FRP measurements with the radius of the circles representing the magnitude of the FRP  
 351 (arbitrary unit). Only measurements with TROPOMI NO<sub>2</sub> quality flag values > 0.5 are shown.  
 352 The regridding of tropospheric NO<sub>2</sub> column was done using a python based coregistration  
 353 algorithm (M. Sneep, KNMI, personal communication, 2023; available on request). Pixels in  
 354 which the cloud pressure was within 4% of the surface pressure were also included to in  
 355 particular allow for pixels with enhanced NO<sub>2</sub> over low altitude smoke, following van der A et  
 356 al. (2020).



357 Fig. 2 shows TROPOMI observations over the same region as Fig. 1 (upper panel). Many  
358 fire emission plumes can be discerned in tropospheric NO<sub>2</sub>, CO and the AAI data. On close  
359 inspection the plumes generally emanate from where SUOMI-NPP FRP indicates fire events  
360 (wind direction was east-north-east). Close to fires tropospheric NO<sub>2</sub> is enhanced which rapidly  
361 drop to background column values typically within 5-10 TROPOMI pixels, approximately 25-  
362 50 km distance and reflecting the relative short lifetime of tropospheric NO<sub>2</sub> of a few hours at  
363 maximum in this moist and sunlit region. For CO and the AAI the plumes extend much further  
364 reflecting the much longer lifetime of both parameters relative to tropospheric NO<sub>2</sub>. On the  
365 timescales of plume advection (hours to a day) CO and AAI act as passive tracers with plume  
366 variations dominated by turbulence and dispersion. For tropospheric NO<sub>2</sub> photochemical  
367 equilibrium and chemical loss also plays a role. The tropospheric NO<sub>2</sub> data also reveal that for  
368 large AAI values and thus optically thick smoke no accurate tropospheric NO<sub>2</sub> column values  
369 (low quality flag value) could be retrieved even though total NO<sub>2</sub> data do show enhanced total  
370 NO<sub>2</sub> over the smoke (not shown). Thick smoke is considered a cloud in the tropospheric NO<sub>2</sub>  
371 retrieval algorithm, hence the low data quality flag value.

372 Fig. 3 show the 2-D probability distributions of daily TROPOMI NO<sub>2</sub>, CO, and AAI for  
373 the large Amazon region of Fig. 1 for the entire month of September. As expected based on  
374 Fig. 2, CO and AAI correlate well whereas tropospheric NO<sub>2</sub> hardly correlates with either.



375 Comparing these distributions for different months for the same region in 2019 and 2020 shows

376 that August and September are the dominant Amazon fire months (see Appendix Fig. A4).

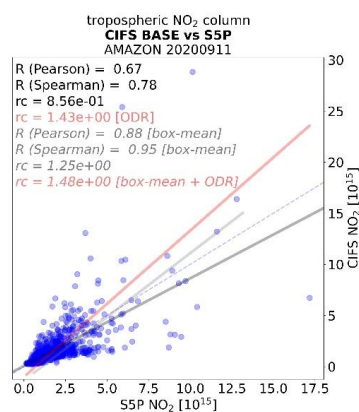
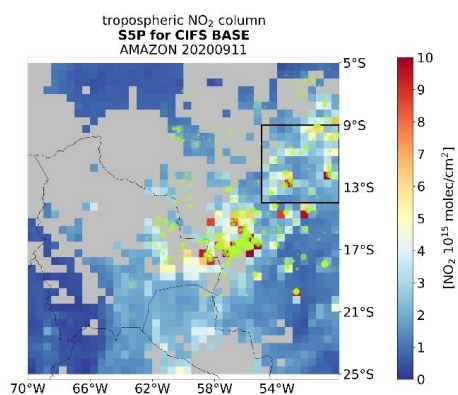
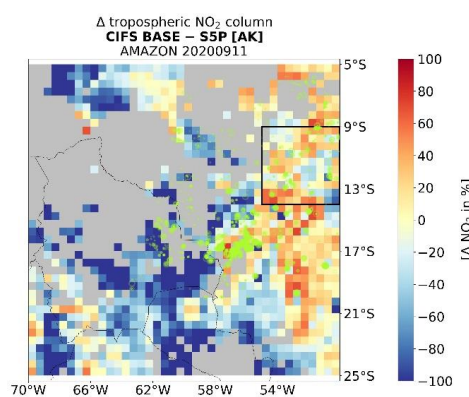
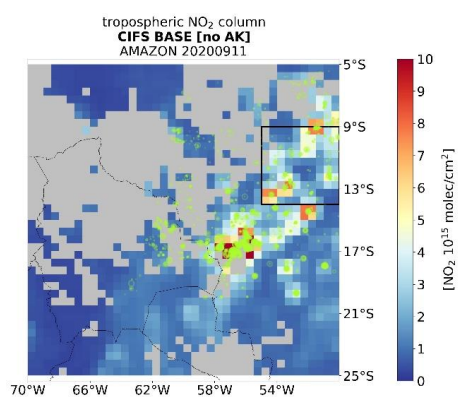
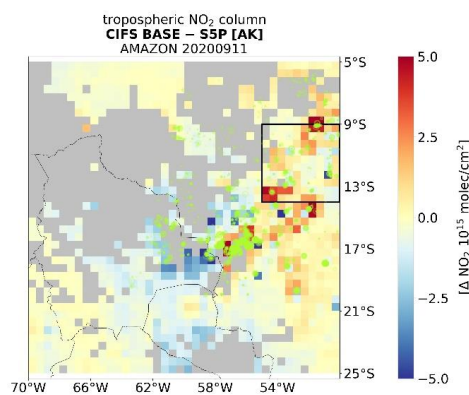
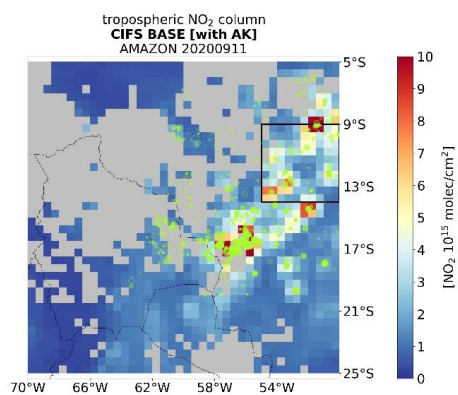
377 **Figure 3.** 2D histogram of daily September 2020 TROPOMI data for AAI and CO (upper

378 panel), CO and NO<sub>2</sub> (middle panel) and AAI and NO<sub>2</sub> (lower panel) for the same region as



379 shown in Fig. 2. For the upper panel the AAI and CO data are biases corrected on a daily basis,  
380 *i.e.* each day the median value of the daily probability distribution is subtracted. See Appendix  
381 Fig. A3 for the same figure without the bias correction. NO<sub>2</sub> data is not bias corrected (middle  
382 and lower panel) and CO data for the lower panel is also not corrected, see Appendix Fig. A3  
383 for the same figure with the CO bias correction as applied for the upper panel of Fig. 3 here.  
384 AAI data is unitless, CO data is in 10<sup>18</sup> molecules cm<sup>-2</sup>, NO<sub>2</sub> data is in 10<sup>15</sup> molecules cm<sup>-2</sup>

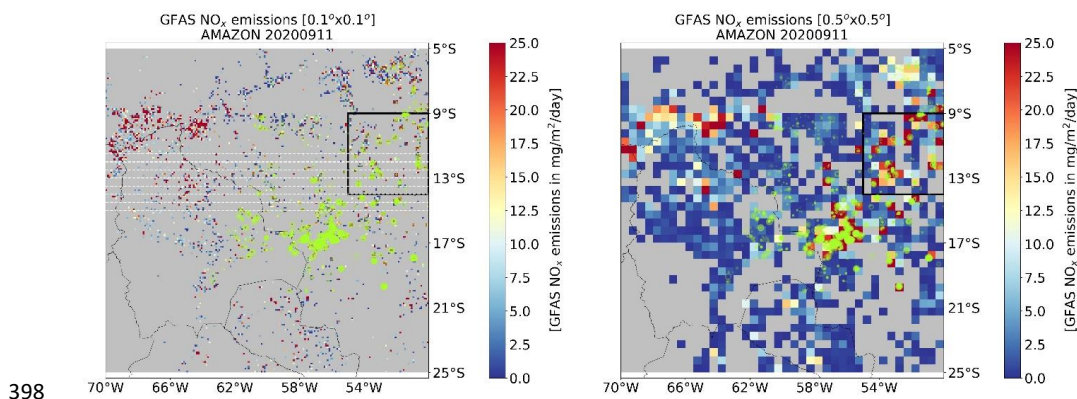




385



386 **Figure 4.** Tropospheric NO<sub>2</sub> columns for the larger Amazon region (Fig. 1, lower panel) for  
387 the IFS-COMPO simulation using GFAS emissions and applying the corresponding  
388 TROPOMI NO<sub>2</sub> averaging kernel (upper left) and without applying the averaging kernel  
389 (middle left) with the corresponding IFS-COMPO grid averaged tropospheric NO<sub>2</sub>  
390 observations (lower left). Differences between IFS-COMPO and TROPOMI in the upper right  
391 panel (absolute) and middle right panel (relative) and corresponding scatter plot and associated  
392 statistics (lower right panel). The small region from Fig. 1 are indicated by the black box.  
393 SUOMI-NPP VIIRS FRP are in the bright green circles as in Fig. 2. The statistics in the lower  
394 right plot display the correlation coefficients for all data points (Pearson's and Spearman's);  
395 the corresponding ordinary linear regression and orthogonal distance regression (ODR; in red);  
396 and the same statistics but for observations averaged in twenty equally distributed TROPOMI  
397 data intervals (“box mean”; in grey and in italics).



399 **Figure 5.** GFAS emissions at 0.1°×0.1° (lower plot) and summed at 0.5°×0.5° right plot for  
400 the large Amazon region as shown in Fig. 1 (lower panel).

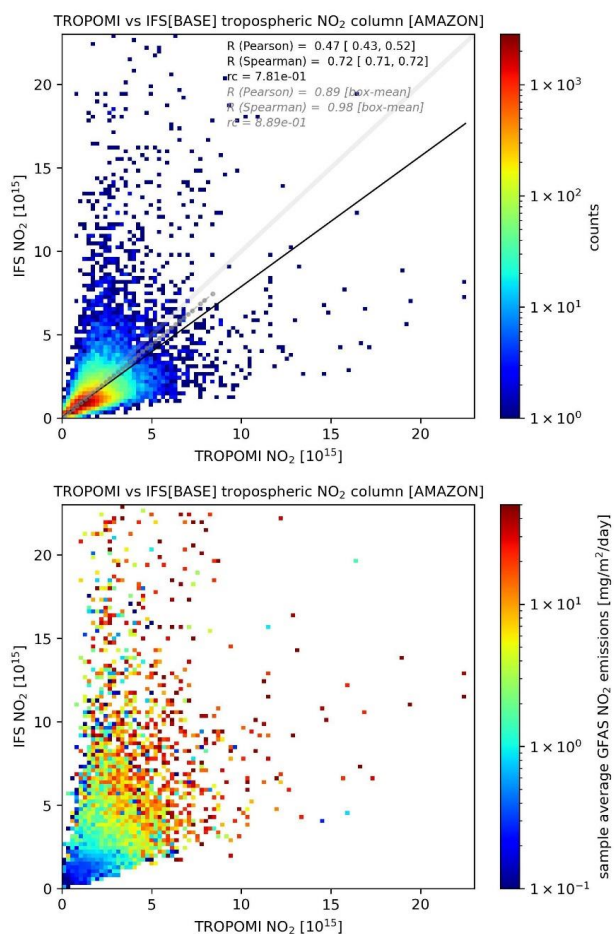
401 Fig. 4 shows a comparison of the IFS-COMPO model simulation configured with its default  
402 settings as also operated in CAMS (GFAS emissions displayed in Fig. 5) and TROPOMI  
403 observed tropospheric NO<sub>2</sub> columns for the same day and large Amazon region as in Fig. 1.



404 There is a reasonable correlation between observed and modeled tropospheric NO<sub>2</sub> columns  
405 (0.67 and 0.78 for respectively  $R^{\text{PEARSON}}$  and  $R^{\text{SPEARMAN}}$ ) but the associated orthogonal linear  
406 regression coefficient (RC) is significantly larger than one (1.43). Averaging tropospheric NO<sub>2</sub>  
407 column data to account for the spread in the distribution of data points improves the correlations  
408 (0.88/0.95) but the large RC remains (1.8). For this day there is a cluster of fires and plumes  
409 south and southwest (14°S-18°S, 60°W-50°W) of the smaller Amazon region of Fig. 1 where  
410 all IFS-COMPO values overestimate tropospheric NO<sub>2</sub>. On the other end, outside of major fire  
411 areas IFS-COMPO tends to underestimate observed tropospheric NO<sub>2</sub>, possibly linked to soil  
412 NO<sub>x</sub> emissions, which will be discussed later. The difference plots show that locally differences  
413 between model simulations and observations can easily be 100% or more.

414 To explore the presence of systematic biases all collocated daily data for August and  
415 September 2020 for the larger Amazon region of Fig. 1 were combined into 2D histograms  
416 shown in Fig. 6. The statistics reveal a fair correlation of 0.47 and 0.72 with a relatively small  
417 uncertainty range and a RC of almost 0.80. Averaging data similar as done in Fig. 4 improves  
418 the comparison with correlations of 0.88 and 0.97 and a larger orthogonal linear RC of 0.90.  
419 More or less similar numbers are found for the smaller Amazon region. Visual inspection of  
420 Fig. 6, however, reveals that there is a significant model bias for large tropospheric NO<sub>2</sub>  
421 columns, *i.e.* IFS-COMPO overestimates tropospheric NO<sub>2</sub> columns and differences can be  
422 multiple factors up to an order of magnitude or more. The opposite, IFS-COMPO more than  
423 an order of magnitude smaller than TROPOMI hardly occurs (see Appendix Table A1).  
424 Strongly enhanced IFS-COMPO tropospheric NO<sub>2</sub> column values in this region are  
425 predominantly associated with fire emissions rather than emissions from other sources. Hence,  
426 the IFS-COMPO “large tropospheric NO<sub>2</sub> column” bias is thus associated with larger fire  
427 emissions.





428

429 **Figure 6.** 2D histogram of TROPOMI observed and IFS-COMPO simulated tropospheric NO<sub>2</sub>  
 430 columns for daily observations throughout August and September 2020 for the larger amazon  
 431 region (Fig. 1). The black line indicates the regression coefficient for all data, the grey line  
 432 (“box-mean”) when IFS-COMPO data are averaged within twenty TROPOMI bins (only with  
 433 more than ten data points in a particular TROPOMI bin). The lower panel displays the same  
 434 distribution as in the upper panel but color coded according to the average GFAS NO<sub>2</sub> emission.  
 435 Note that distributions between both differ slightly as occasionally for a TROPOMI - IFS-  
 436 COMPO comparison the corresponding GFAS emissions are zero (used in the lower plot).



437 To further explore this IFS-COMPO “large tropospheric NO<sub>2</sub> column” bias a number of  
438 IFS-COMPO model experiments were performed (see Tables 1 and 2 and Appendix Table A1).

439 Replacing the GFAS fire NO<sub>x</sub> emissions in IFS-COMPO with GFA NO<sub>x</sub> emissions  
440 (experiments GFA, GFA.IFSCYCLE, GFA.SOIL; Appendix Fig. A5) resulted in larger  
441 observed differences. Although correlations remained similar, lower regression coefficients  
442 indicate larger differences between observations and model outcomes.

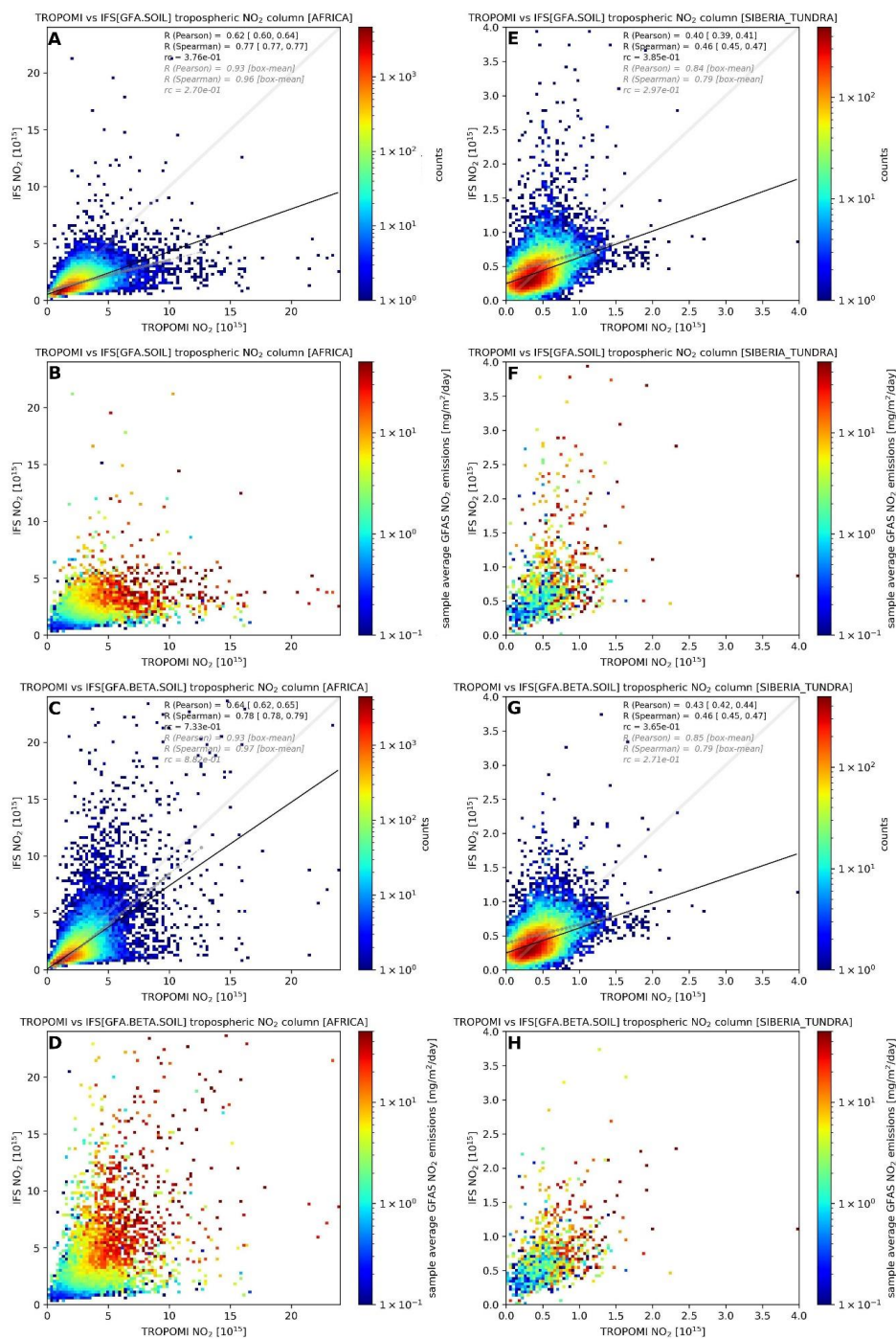
443 Another test was to put a hard cap on NO<sub>x</sub> emissions (see Appendix Fig. A6). For  
444 BASE.CAP0.1 the NO<sub>x</sub> emission cap was set at  $1 \cdot 10^{-10}$  kg m<sup>-2</sup> s<sup>-1</sup> (~0.1 mg m<sup>-2</sup> d<sup>-1</sup>), for  
445 BASE.CAP0.3 this was  $3 \cdot 10^{-10}$  kg m<sup>-2</sup> s<sup>-1</sup> (~0.3 mg m<sup>-2</sup> d<sup>-1</sup>; both with GFAS emissions) while  
446 for GFA.CAP0.3 the same  $3 \cdot 10^{-10}$  kg m<sup>-2</sup> s<sup>-1</sup> emission cap was used but for the GFA-S4F  
447 emissions. Although capping the emissions obviously reduces the presence of the “large  
448 tropospheric NO<sub>2</sub> column” bias it did not significantly improve the correlation and even  
449 worsened the regression coefficients.

450 An alternative approach was to directly use TROPOMI NO<sub>2</sub> column data to constrain  
451 emissions (BASE.BETA, GFA.BETA; Appendix Figs. A6 and A7) using the β-method that  
452 was introduced in section 2.5. This indeed improves the regression results and especially for  
453 the GFA-S4F emissions the “large tropospheric NO<sub>2</sub> column” bias is strongly reduced (number  
454 of strongly deviating IFS-COMPO pixels reduced by an order of magnitude) with orthogonal  
455 linear regression coefficients much more in line with the baseline results for GFAS (BASE):  
456 for instance, the spearman correlation coefficient is 0.75 for both experiments with the β-  
457 method applied, where it was 0.60 for the reference GFAS experiment (Table 1). The fact that  
458 overall very similar results are achieved with the β-method, independent of the prior emissions,  
459 gives confidence in its procedure which to first order is independent of the prior emissions.  
460 Nevertheless, these experiments fail in improving the RC (RC = 0.729, 0.739 for experiments



461 with  $\beta$ -method, and  $RC = 0.764$  for the BASE experiment), pointing at a common negative  
462 model bias largely independent of fire emissions.

463 These results indicate that a large portion of the remaining negative model bias was not  
464 affected and optimized during the fire  $NO_x$  optimization procedure, and therefore is likely  
465 attributed to other emissions than fires. In particular the soil  $NO_x$  emissions in the default  
466 configuration of IFS-COMPO CY48R1 are identified to be comparatively low. For that reason  
467 a set of IFS-COMPO simulations was performed with updated soil  $NO_x$  emissions, both  
468 without, and with optimized fire  $NO_x$  emissions (IFS-COMPO experiments GFA.SOIL and  
469 GFA.BETA.SOIL see Table 1, Appendix Figs. A5 and A7). Solely updating the soil  $NO_x$   
470 emissions had a limited effect on the statistics ( $RC = 2.15$  in GFA.SOIL vs. 2.11 in  
471 GFA.IFSCYCLE), indicating that the biases due to fire  $NO_x$  emissions in GFA-S4F are  
472 dominating. But combined with  $\beta$ -optimization the statistics improved and especially the  
473 orthogonal linear regression coefficients approached the value of one ( $RC = 0.953$  in  
474 GFA.BETA.SOIL, vs 0.939 in GFA.BETA).





476 **Figure 7.** Panels (A, B) as Fig. 6 but for the Africa region (10°E-30°E and 5°S-25°S). IFS-  
477 COMPO simulations with GFAS emissions and updated soil NO<sub>x</sub> emissions; panels (C, D) as  
478 panels (A, B) but with  $\beta$ -optimized GFAS emissions; panels (E, F) as panels (A, B) but for the  
479 Siberia tundra region (125°E-145°E, 55°N-75°N); panels (G, H) as panels (A, B) but with  $\beta$ -  
480 optimized GFAS emissions for the Siberia tundra region (125°E-145°E, 55°N-75°N).

### 481 **3.2 Other regions: sub-equatorial African savannahs, Siberian steppes and tundra**

482 The quality of GFAS fire NO<sub>x</sub> emissions, and the optimization based on the  $\beta$ -method was  
483 further explored for a selection of other regions (a sub-equatorial region in Africa, a Siberia  
484 tundra region and a Siberia steppe region, see Appendix Fig. A2). This choice was motivated  
485 by the very different vegetation types, soils characteristics and weather and climatological  
486 conditions of each region: sub-equatorial Africa fires are dominated by savannahs and arid  
487 shrublands; the Siberia tundra fires are dominated by wet evergreen forest and tundra  
488 vegetation; the Siberian steppe fires are dominated by vast grasslands. They therefore provide  
489 clues as to whether the agreement and discrepancies found for the Amazon/Cerrado region  
490 generally hold or are just a regional phenomenon. For these other regions we solely rely on the  
491 IFS-COMPO simulations with GFAS emissions and updated soil NO<sub>x</sub> emissions while  
492 comparing results with and without  $\beta$ -optimization. Table 2 summarized the results for these  
493 three regions.

494 For sub-equatorial Africa (Fig. 7 panels A – D), observed and modeled tropospheric NO<sub>2</sub>  
495 columns have a similar dynamical range, a similar spread and variability, and a similar  
496 dependence of larger tropospheric NO<sub>2</sub> columns over regions with larger emissions. However,  
497 the IFS-COMPO simulations significantly and systematically underestimate tropospheric NO<sub>2</sub>  
498 columns



IFS run ID	region	IFS setup	emissions	all data		averaged data	
				R <sup>PEARSON</sup> [CI] R <sup>SPEARMAN</sup> [CI]	RC	R <sup>PEARSON</sup> R <sup>SPEARMAN</sup>	RC
Nitrogen Dioxide (NO <sub>2</sub> )							
b2em GFA.SOIL	Africa	updated soil NO <sub>x</sub>	GFA-S4F	0.62 [0.60, 0.64] 0.77 [0.77, 0.77]	0.376	0.93 0.96	0.270
b2ew GFA.BETA.SOIL	Africa	updated soil NO <sub>x</sub> β-optimized emissions	GFA-S4F	0.64 [0.62, 0.65] 0.78 [0.78, 0.78]	0.733	0.93 0.97	0.882
b2em GFA.SOIL	Siberia-tundra	updated soil NO <sub>x</sub>	GFA-S4F	0.40 [0.39, 0.41] 0.46 [9.45, 0.47]	0.385	0.84 0.79	0.297
b2ew GFA.BETA.SOIL	Siberia-tundra	updated soil NO <sub>x</sub> β-optimized emissions	GFA-S4F	0.43 [0.42, 0.44] 0.46 [0.45, 0.47]	0.365	0.85 0.79	0.271
b2em GFA.SOIL	Siberia-steppe	updated soil NO <sub>x</sub>	GFA-S4F	0.62 [0.61, 0.63] 0.65 [0.64, 0.65]	0.493	0.96 0.99	0.556
b2ew GFA.BETA.SOIL	Siberia-steppe	updated soil NO <sub>x</sub> β-optimized emissions	GFA-S4F	0.62 [0.61, 0.63] 0.65 [0.64, 0.65]	0.494	0.97 0.99	0.555
Carbon Monoxide (CO)							
b2bd BASE	Amazon		GFASv1.4	0.88 [0.88, 0.88] 0.94 [0.94, 0.94]	0.571	0.89 0.86	0.351
b2bj GFA	Amazon		GFA-S4F	0.87 [0.87, 0.88] 0.93 [0.93, 0.94]	0.792	0.92 0.99	1.020
b2bd BASE	Africa		GFASv1.4	0.64 [0.61, 0.66] 0.75 [0.74, 0.76]	0.292	0.98 0.99	0.300
b2bd BASE	Siberia-tundra		GFASv1.4	0.74 [0.73, 0.74] 0.83 [0.83, 0.83]	0.694	0.93 0.97	0.428
b2bd BASE	Siberia-steppe		GFASv1.4	0.78 [0.78, 0.79] 0.75 [0.75, 0.76]	0.358	0.97 1.00	0.361



500 **Table 1.** Overview of statistics of the comparison of IFS-COMPO simulated and TROPOMI  
501 observed tropospheric NO<sub>2</sub> column over the larger Amazon region (like Figs. 6-7-8). All  
502 simulations used the CBM5 atmospheric chemistry scheme. Several simulations also make use  
503 of a subgrid-scale emission plume chemistry-dispersion parameterization scheme (SGS) that  
504 accounts for the fact that most emission plumes are significantly smaller than the CAMS/CIFS  
505 grid size, and that plume chemistry thus is a subgrid scale process. Sensitivity tests revealed  
506 that this subgrid scale parameterization had only minor impacts on simulated NO<sub>2</sub> and CO.  
507 Box-mean data refers to the statistics of the average values. The four-character IDs refers to  
508 the ECMWF supercomputer simulations and are included here for traceability purposes.  
509



IFS run ID	IFS setup	emissions	IFS version	$R^{PEARSON}$ [CI] $R^{SPEARMAN}$ [CI]	RC	$R^{PEARSON}$ $R^{SPEARMAN}$	RC
b2bd BASE	“large Amazon region”	GFASv1.4	CY47R3.1	0.47 [0.44, 0.52] 0.72 [0.72, 0.73]	0.798	0.88 0.97	0.900
b2bd BASE	“small Amazon region”	GFASv1.4	CY47R3.1	0.57 [0.53, 0.62] 0.60 [0.58, 0.62]	0.764	0.94 0.94	0.820
b2by BASE.CAP0.1	NO <sub>x</sub> emissions capped $1 \cdot 10^{10}$ kg m <sup>-2</sup> s <sup>-1</sup>	GFASv1.4	CY47R3.1	0.64 [0.63, 0.65] 0.70 [0.69, 0.70]	0.304	0.93 0.94	0.227
b2c4 BASE.CAP0.3	NO <sub>x</sub> emissions capped $3 \cdot 10^{10}$ kg m <sup>-2</sup> s <sup>-1</sup>	GFASv1.4	CY47R3.1	0.63 [0.62, 0.64] 0.72 [0.71, 0.72]	0.473	0.96 0.96	0.421
b2bj GFA		GFA-S4F	CY47R3.1	0.36 [0.34, 0.40] 0.73 [0.72, 0.73]	2.230	0.86 0.96	3.340
b2c6 GFA.CAP0.3	NO <sub>x</sub> emissions capped $3 \cdot 10^{10}$ kg m <sup>-2</sup> s <sup>-1</sup>	GFA-S4F	CY47R3.1	0.59 [0.57, 0.61] 0.74 [0.73, 0.74]	0.623	0.94 0.94	0.577
b2d3 GFA.IFSCYCLE		GFA-S4F	CY48R1.0 SGS	0.35 [0.32, 0.39] 0.73 [0.73, 0.74]	2.110	0.85 0.99	3.210
b2dl BASE.BETA	β-optimized emissions	GFASv1.4	CY48R1.0 SGS	0.50 [0.44, 0.61] 0.75 [0.74, 0.75]	0.729	0.86 0.98	0.868
b2dz GFA.BETA	β-optimized emissions	GFA-S4F	CY48R1.0 SGS	0.41 [0.36, 0.49] 0.75 [0.75, 0.76]	0.739	0.97 0.98	0.752
b2em GFA.SOIL	updated soil NO <sub>x</sub>	GFA-S4F	CY48R1.0 SGS	0.36 [0.33, 0.40] 0.75 [0.74, 0.75]	2.150	0.86 0.99	3.230
b2ew GFA.BETA.SOIL	updated soil NO <sub>x</sub> β-optimized emissions	GFA-S4F	CY48R1.0 SGS	0.36 [0.31, 0.43] 0.78 [0.77, 0.78]	0.953	0.95 0.98	1.04





511 **Table 2.** As Table 1 but for baseline simulations and other regions for both tropospheric NO<sub>2</sub>  
512 and CO. All simulations used the CBM5 atmospheric chemistry scheme and the subgrid-scale  
513 emission plume chemistry-dispersion parameterization (SGS, see caption Table 1).

514	* Amazon “large”	= 70°W - 50°W	25°S-5°S
515	* Amazon “small”	= 55°W - 50°W	14°S-9°S
516	* Africa	= 10°E - 30°E	25°S-5°S
517	* Siberia-tundra	= 125°E - 145°E	55°N-75°N
518	* Siberia-steppe	= 40°E - 60°E	40°N-60°N

519

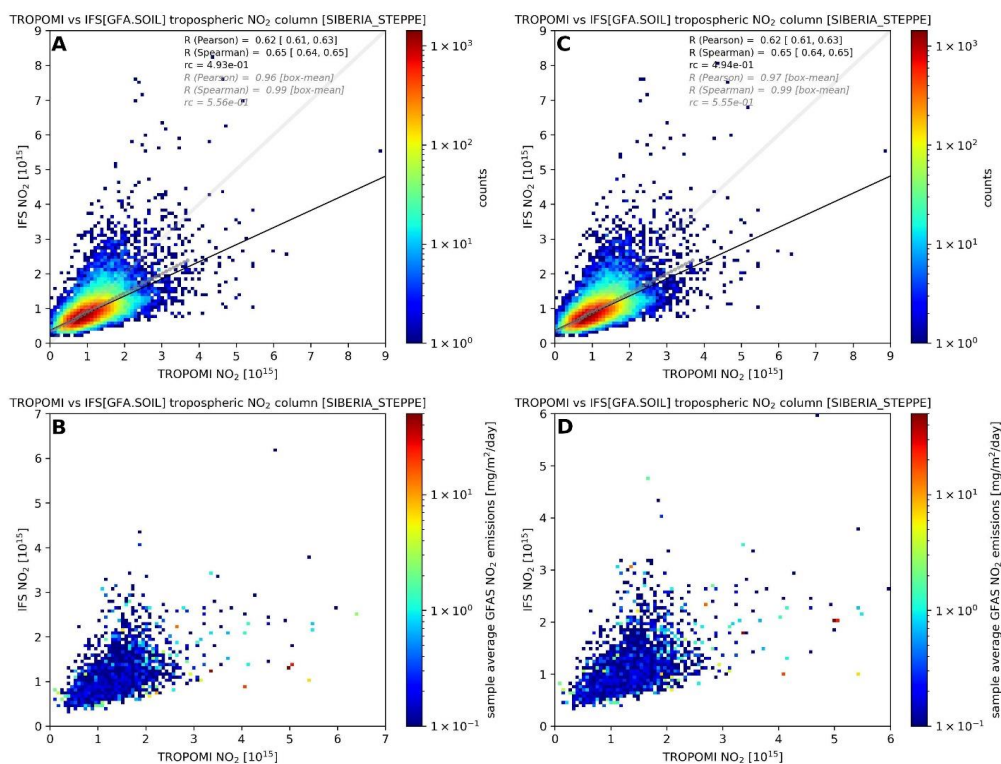
520 which is opposite from the Amazon/Cerrado region. Updating GFAS emissions using the  $\beta$ -  
521 optimization significantly improves the comparison, in particular the regression coefficient.

522 For Siberia the conditions are very different from those in the Amazon and Africa. First of  
523 all, the dynamical range of tropospheric NO<sub>2</sub> columns is much smaller (compare Figs. 6 and  
524 Fig. 7 panels E – H and Fig. 8 panels A - D) and there are fewer fires as evidenced by a limited  
525 number of points outside of the main probability distribution. Especially for the Siberia Steppe  
526 region fire emissions are very small. Although both Siberia regions show a tropospheric NO<sub>2</sub>  
527 column bias not dissimilar from those in Africa, applying the  $\beta$ -optimization does not result in  
528 a large improvement unlike for the Amazon and Africa regions. Given that there are fewer fires  
529 in Siberia in the particular period studied here, this may not be that surprising as there are not  
530 many fire-affected regions and thus tropospheric NO<sub>2</sub> columns to  $\beta$ -optimize. Note that the  
531 tropospheric NO<sub>2</sub> columns for Siberia (especially tundra) and fire NO<sub>2</sub> emissions are much  
532 smaller than those for the Amazon/Cerrado and Africa. Which is unlike CO for which column  
533 values and emissions are comparable (see next section, Table 2 and Appendix Fig. A8). This  
534 reflects differences in fire characteristics: boreal vegetation is wetter and burning will be more



535 incomplete (more CO and smoke) and at much lower temperatures (less NO<sub>2</sub>) (Andreae, 2019;

536 van Wees et al., 2022).



537

538 **Figure 8.** Panels (A, B) as Fig. 6 but for the S4F Siberia steppe region (40°E-60°E, 40°N-

539 60°N); panels (C, D) as panels (A, B) with β-optimized GFAS emissions but for the S4F

540 Siberia steppe region (40°E-60°E, 40°N-60°N)

### 541 3.3 Carbon Monoxide

542 Next we present the comparison of the IFS-COMPO simulations of CO – see further Table

543 2. In this case the number of IFS-COMPO tests was limited to comparing IFS-COMPO either

544 with GFAS or GFA CO emissions. Overall, for all regions there is a good correlation between

545 modeled and observed total CO columns, better than for NO<sub>2</sub>. This likely reflects the simpler

546 chemistry and longer lifetime of CO, causing CO to vary on larger spatial scales that are easier



547 for IFS-COMPO to capture. For all regions IFS-COMPO nevertheless consistently and  
548 significantly underestimates CO columns by 20-70%. However, and importantly, the  
549 regression coefficient when using GFA-S4F emissions over the Amazon region significantly  
550 improves the comparison to the level that the observations and model results compare very  
551 well. A small bias may remain but given that the GFA-S4F CO emission data was only  
552 available over the Amazon region and for example not the entire South American continent  
553 and combined with the long CO lifetime the remaining small bias may simply be the results of  
554 lack of updating emissions outside of the S4F Amazon region (missing advection of additional  
555 CO outside of the area of interest). This suggests that despite the larger bias in terms of NO<sub>2</sub>,  
556 the prior emission estimates of dry-matter burned in GFA-S4F over the amazon are likely better  
557 than GFAS, and the discrepancy with respect to TROPOMI NO<sub>2</sub> points rather at uncertainties  
558 in the NO<sub>x</sub> emission factor.

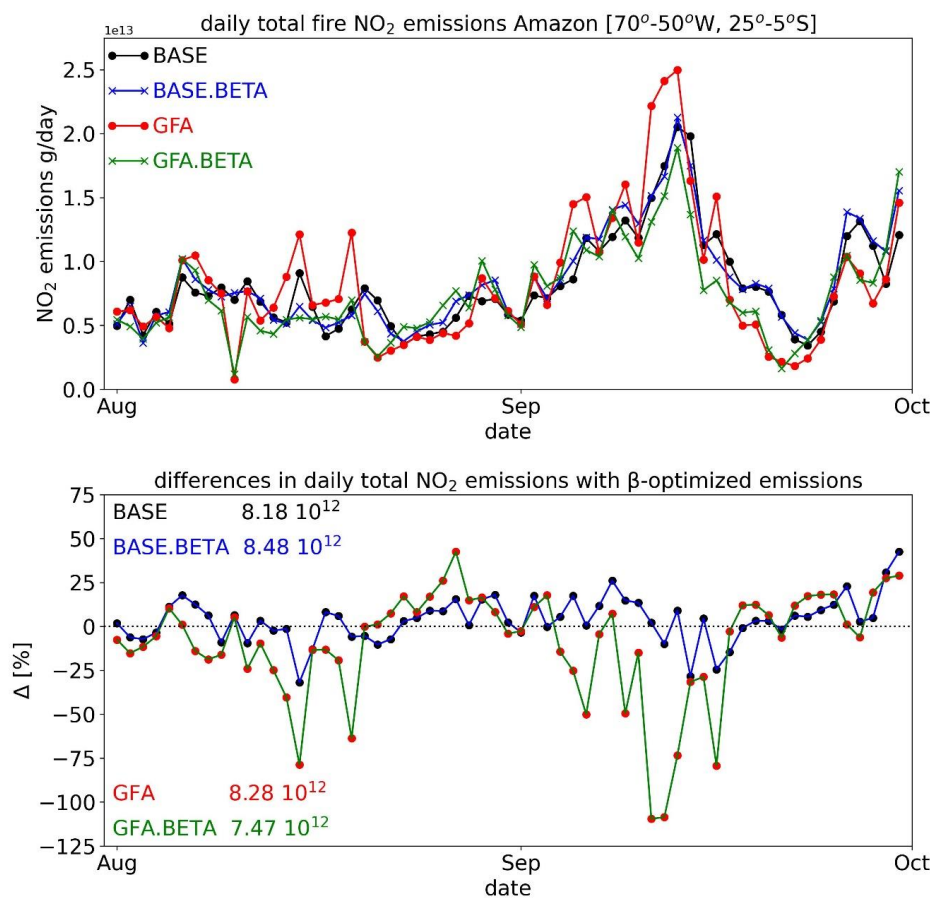
### 559 **3.4 Time series**

560 Finally, a key question regarding the fire NO<sub>2</sub> emissions results discussed here is how much  
561 in particular the “large tropospheric NO<sub>2</sub> column” bias really matters. To answer that question,  
562 Fig. 9 shows the daily total NO<sub>2</sub> emissions for the Amazon region for four different emission  
563 databases: GFAS, GFA-S4F and the  $\beta$ -optimized emissions for both.

564 The comparison first reveals that the temporal variability in NO<sub>2</sub> emissions for the Amazon  
565 in GFAS and GFA-S4F are very comparable. There are some differences, but overall temporal  
566 variability in emissions as well as the amplitude of emissions are similar. The second notable  
567 result is that the  $\beta$ -optimization has a significant impact on in particular the GFA-S4F NO<sub>2</sub>  
568 emissions, and provides results that are very similar compared to the other estimates (GFAS  
569 and GFAS  $\beta$ -optimized) in terms of temporal variability, while the area-and time-averaged  
570 emission totals, quantified in terms of daily mean emissions, are overall reduced. It was shown



571 previously that the GFA-S4F NO<sub>2</sub> emissions significantly worsened “large tropospheric NO<sub>2</sub>  
572 column” bias. The  $\beta$ -optimization nevertheless can largely correct for this bias. This is a  
573 valuable result as it allows - at least to first order – to independently provide an estimate of the  
574 fire NO<sub>x</sub> emissions based on TROPOMI observations for evaluation and verification of bottom-  
575 up emission databases. The impact of the “large tropospheric NO<sub>2</sub> column” bias on emission  
576 totals nevertheless is rather small. Total NO<sub>x</sub> emissions differ on average by 10% or less. That  
577 indicates that not only a small subset of larger fires which appear over-estimated in GFA-S4F  
578 is important to match the emission totals, but also a larger, dominating subset of smaller fires,  
579 with low NO<sub>x</sub> emissions, which may be under-estimated in GFA-S4F.



580

581 **Figure 9.** Daily total NO<sub>2</sub> emissions over the larger Amazon region for August and  
 582 September 2020. GFAS emissions in black (BASE), β-optimized GFAS emissions in blue  
 583 (BASE.BETA), GFA emissions in red (GFA), β-optimized GFA emissions in green  
 584 (GFA.BETA).

585 For Africa and the Siberia tundra regions – where only a comparison with β-optimized  
 586 emission is available for GFAS data – results are similar (Appendix Fig. A9). For the Siberia  
 587 steppe region absolute emissions (~0.11-0.12 Tg day<sup>-1</sup>) are approximately an order of



588 magnitude smaller compared to those for the Siberia tundra region ( $0.75 \text{ Tg day}^{-1}$ ) and  
589 approximately two orders of magnitude smaller than those for Africa and the Amazon ( $\sim 8 \text{ Tg}$   
590  $\text{day}^{-1}$ ). Comparing the various emission datasets with TROPOMI tropospheric  $\text{NO}_2$   
591 observations reveal a fair to strong spatial correlation ranging between 0.568 and 0.993  
592 depending on emission database and regions ( $R^2$ , Pearson and Spearman; see Appendix Table  
593 A2), except for the Siberia steppe region. This reflects the limited number of fires in the Siberia  
594 steppe region and a limited number of days for the Siberian steppe region where  $\beta$ -optimized  
595 emissions differ from the GFAS emissions (Appendix Fig. A9) indicating that for most days  
596 there are no fires and thus no  $\text{NO}_x$  emission updates.

#### 597 **4. Discussion**

598 Using bottom-up fire  $\text{NO}_x$  and CO emission estimates in the IFS-COMPO model and then  
599 comparing results with TROPOMI data revealed the existence of two significant biases in  
600 bottom-up emission estimates. GFAS emissions were used as a “state of the art” global fire  
601 emission database, the emission data developed in the S4F project in order to update bottom-  
602 up fire emissions using remote sensing data not used in for example GFAS.

603 Overall, the results of the Amazon IFS  $\text{NO}_x$  simulations and sensitivity tests can be  
604 summarized as follows.

- 605 • IFS-COMPO simulations with GFAS emissions results in an overestimation of  
606 tropospheric  $\text{NO}_2$  columns over fire regions, especially for large fires, the so-called “large  
607 tropospheric  $\text{NO}_2$  column” bias
- 608 • IFS-COMPO simulations with GFAS systematically underestimate background  
609 tropospheric  $\text{NO}_2$  columns, possibly pointing to an underestimation of soil  $\text{NO}_x$  emissions



- 610 • IFS-COMPO simulations GFA-S4F emissions worsen the “large tropospheric NO<sub>2</sub>
- 611 column” bias resulting in a significantly larger structural IFS-COMPO NO<sub>2</sub> column bias
- 612 • capping the NO<sub>x</sub> emissions largely reduces the “large tropospheric NO<sub>2</sub> column” bias but
- 613 worsens the statistics, in particular the regression of modeled vs. observed tropospheric
- 614 NO<sub>2</sub> columns
- 615 • optimizing the fire NO<sub>2</sub> emissions based on TROPOMI NO<sub>2</sub> observations using the IFS-
- 616 based  $\beta$ -method drastically improves the IFS-COMPO results, in particular for the GFA-
- 617 S4F emissions, but does not completely close the gap between model and TROPOMI
- 618 observations
- 619 • updating the soil emissions alone does not improve the IFS-COMPO simulations results
- 620 • combining the  $\beta$ -optimized fire emissions together with updated soil NO<sub>x</sub> emissions yielded
- 621 the best results both in terms for correlations and regression coefficients

622 Note that the persistent “large-tropospheric-NO<sub>2</sub>-column” bias regardless of using GFAS or  
623 GFA-S4F emissions implies its cause is not satellite-data based vegetation characteristics but  
624 possibly emission factors that are used to translate these vegetation characteristics to trace gas  
625 emission amounts. For example, NO<sub>x</sub> emissions associated with burning and combustion are  
626 strongly temperature dependent and highly non-linear. Only when combustion takes place at  
627 very high temperatures larger than 1500° Celsius can N<sub>2</sub> break down into atomic N that can  
628 recombine with O<sub>2</sub> to form NO and NO<sub>2</sub>, the so-called Zeldovich mechanism. These are  
629 temperatures associated with the blue-flaming phase of fires. Given that laboratory  
630 measurements of fire NO<sub>x</sub> emission factors necessarily are restricted to small fires it is  
631 conceivable that those emission factors are not representative for large fires. Jin et al. (2021)  
632 recently showed that - using TROPOMI NO<sub>2</sub> data - fire NO<sub>x</sub> emission factors appear much  
633 more variable with a much larger dynamical range than currently assumed and used.



634 Secondly, based on the comparison of IFS-COMPO results and TROPOMI data, CO  
635 emissions were consistently largely underestimated by GFAS for the four regions we explored  
636 (biased low by 20 - 70%) even though the spatial correlation between observed and modeled  
637 CO total columns was very good with correlations ( $R^2$ ) exceeding 0.85 for all regions and cases.  
638 Using the GFA-S4F CO emissions rather than the GFAS emissions for the Amazon improved  
639 the spatial correlation while on average significantly decreasing the bias, possibly even  
640 eradicating the bias depending on the method with which the data was evaluated. That does not  
641 mean all issues were resolved as there was an approximately 25% standard deviation in the  
642 differences of modeled and observed CO total columns indicating that locally discrepancies  
643 between emissions and observations remain. Nevertheless, the results strongly suggest that the  
644 (larger) CO emissions in GFA-S4F are more realistic than those from GFAS. Note that the  
645 underestimation of background values of atmospheric CO is a common problem with many  
646 atmospheric chemistry models (Gaubert et al., 2020), not just IFS-COMPO, and that this  
647 underestimation likely has multiple causes (Inness et al., 2022).

648 Bottom-up fire CO emission estimates have for decades continued to be rather uncertain  
649 for various reasons and despite significant amounts of research on the topic (Andreae, 2021).  
650 Important culprits are the characterization of land cover types, fuel conditions as well as fire  
651 dynamics and weather conditions. For many bottom-up fire-emission parameters there is  
652 insufficient *in situ* data or empirical data and observations to constrain emissions. An important  
653 source of uncertainty is the satellite observation-based characterization of land cover type.  
654 While there are now many satellites observation Earth's surface and many more methods and  
655 approaches to characterize the land cover type, considerable differences between land use and  
656 land cover datasets remain (Liu et al., 2021; see further Khaldi et al. (2022) and references  
657 therein). Another important source of uncertainty are satellite-based fuel loads and fuel





658 conditions. Observations to constrain these parameters are typically only available once every  
659 10 days or worse as clouds can further limit satellite observations of these parameters.

660 Finally, although the first S4F results are very promising towards improving fire emissions,  
661 the approach presented here is built on generic statistics: combining many fires and the effect  
662 of many fires and reduce the analysis results to a few statistics. Although valuable, this  
663 approach does not make optimal use of the rich information density of the satellite data. If  
664 many uncertainties are related to fire specific properties and conditions then further refinement  
665 and analysis of individual fires – as to some extent explored for NO<sub>2</sub> in Jin et al., (2021) -  
666 would be a worthy approach. This, however, requires stepping away from gridded and averaged  
667 data and change thinking towards fires as single and unique spatial structures. Each fire, each  
668 structure, would be associated with specific characteristics: its fuel load, vegetation type(s),  
669 fuel moisture, area, moisture, weather conditions, and emission plume characteristics. The  
670 GFA-S4F data is a step in this direction as the emission data is provided per fire structure  
671 (polygons) and each fire was associated with other fire characteristics from GFA-S4F data  
672 based on Sentinel-2 and Sentinel-3 data. However, for TROPOMI data such an approach is still  
673 lacking. Fire emission plumes would have to be identified first and then linked to a fire.  
674 Automated detection of TROPOMI-based (fire) emission plumes has only started to be  
675 developed in recent years (Kurchuba et al., 2021; Finch et al., 2022; Goudar et al., 2023; Schuit  
676 et al., 2023), especially thanks to the recent advance of data-intensive artificial intelligence  
677 analysis techniques, but has the potential to further advance satellite-data-based estimates of  
678 fire emissions.

## 679 **5. Conclusions.**

680 The Sense4Fire project aims to increase the scientific understanding of fire dynamics and  
681 their role in the carbon cycle by integrating observations from the Sentinels into new Earth



682 observation products. This paper presents a first analysis of TROPOMI satellite observations  
683 of fire plumes affecting atmospheric composition, and the use of trace gas (CO, NO<sub>2</sub>) from  
684 TROPOMI together with IFS-COMPO model simulations and to evaluate and optimize  
685 satellite-based fire CO and NO<sub>x</sub> emissions.

686 TROPOMI allows for observing single fire emission plumes (NO<sub>2</sub>, CO, AAI) on a daily  
687 basis with unprecedented accuracy and spatial resolution. Results show that CO and AAI  
688 correlate very well, but not with NO<sub>2</sub>, related to the much shorter lifetime of NO<sub>2</sub>. Visually  
689 there is also an excellent agreement with VIIRS RGB imagery.

690 The analysis of August-September 2020 daily TROPOMI data and IFS-COMPO model  
691 results over the Amazon/Cerrado region reveal significant biases in bottom-up emission data  
692 of CO and NO<sub>x</sub>. For simulated NO<sub>2</sub> a significant positive bias for large-fire cases over the  
693 Amazon/Cerrado region was identified attributed to the GFAS fire emissions, while CO  
694 emissions were significantly underestimated. Note that total NO<sub>x</sub> emissions are dominated by  
695 small fires with only a small contribution from the few large fires but that this large fire bias is  
696 nevertheless of concern as it reflects a lack of understanding.

697 These biases could not be attributed to the IFS-COMPO model resolution or sub-grid plume  
698 chemistry processes. When using fire emissions from the GFA-S4F system which incorporates  
699 more advanced geo-information that tracks individual fires the evaluations against TROPOMI  
700 CO total columns were significantly improved, but the NO<sub>2</sub> tropospheric column evaluations  
701 worsened by showing an increased positive model bias. This suggests that not only there is a  
702 considerable uncertainty in the dry-matter-burned estimates, but also in the emission factors  
703 that define the ratio between CO and NO<sub>x</sub> emissions.



704 A scaling approach was adopted to constrain bottom-up fire NO<sub>x</sub> emissions with  
705 TROPOMI NO<sub>2</sub> observations, which relies on the local sensitivity of tropospheric NO<sub>2</sub> column  
706 changes with respect to NO<sub>x</sub> emission changes (the  $\beta$ -method). This brought the emission  
707 variability much closer in line with those from GFAS, independent of which prior emission  
708 estimate was used. Feeding any of the optimized fire NO<sub>x</sub> emissions back into the model indeed  
709 led to a significant improvement and disappearance of the positive bias associated to large  
710 emission sources, while the background model bias was unaffected. Combined with improved  
711 soil NO<sub>x</sub> emissions results are on average further improved. This illustrates that emission types  
712 of different origin can be optimized independently, and that both emission types need to be  
713 optimized to match the model simulations with the observations.

714 Overall results presented here show that advanced use of geo-information from the suite of  
715 ESA Sentinel satellites helps improve and constrain fire emissions, although not perse by  
716 relying solely on satellite data-based bottom-up emissions – for instance a careful assessment  
717 of emission factors is needed. On the other hand, the focus of this paper as well as the first  
718 phase of the S4F project has been on average and cumulative statistics. Although those statistics  
719 could be improved, that approach does not address many uncertainties and discrepancies at  
720 local spatial scales and the level of individual fires. Also, in depth understanding of the biases  
721 that were identified is still lacking and requires additional research. Fortunately, the suite of  
722 ESA Sentinel satellites allows for much more detailed in-depth analysis of fires and the S4F  
723 project will be extended to further explore its results and provide more detailed analyses of  
724 fires and their contributing factors.

## 725 **Acknowledgements**

726



727 This research is funded by the ESA Sense4Fire project which is part of the Carbon Science  
728 Cluster of ESA's Scientific Data Exploitation element of the Earth Observation Envelope  
729 Programme (EOEP-5). The Sense4Fire project is funded by ESA under ESA Contract Number:  
730 4000134840/21/I-NB. Sentinel-5 Precursor is a European Space Agency (ESA) mission on  
731 behalf of the European Commission (EC). The TROPOMI payload is a joint development by  
732 ESA and the Netherlands Space Office (NSO). The Sentinel-5 Precursor ground-segment  
733 development has been funded by ESA and with national contributions from The Netherlands,  
734 Germany, and Belgium. This work contains modified Copernicus Sentinel-5P TROPOMI data  
735 (2018-2022), processed in the operational framework or locally at KNMI.

736

737 The authors thank - in alphabetical order - Alfred Awotwi (Cardiff University), Daniel  
738 Kinalczyk, Christopher Marrs and Christine Wessollek (Technical University Dresden) as well  
739 as ESA project officer Stephen Plummer for their contributions within the S4F project that led  
740 to this paper.

741

742 *Author contributions.* A.d.L. wrote the paper and did the majority of data analysis and  
743 interpretation. V.H. performed the IFS-COMPO model simulations while N.A. provided GFA  
744 emission data. M.F., V.H and N.A. all reviewed the paper and contributed to the discussion  
745 and interpretation of results.

746

747 *Competing interests.* The authors declare that they have no conflicts of interest.

748

749 *Data availability.* TROPOMI data used in this paper is available via the EU COPERNICUS  
750 data space or Amazon Web Services. GFA emission data is available via de Global Fire Data  
751 webportal. GFAS emission data is available via the EU COPERNICUS atmosphere data store.



752 IFS-COMPO model simulations are stored in the ECMWF archives and can be made available  
753 on request.

754 <https://dataspace.copernicus.eu/>

755 <https://registry.opendata.aws/sentinel5p/>

756 <https://www.globalfiredata.org/>

757 <https://ads.atmosphere.copernicus.eu/>

758

## 759 **References**

760 van der A, R. J., de Laat, A. T. J., Ding, J. and Eskes, H. J.: Connecting the dots: NO<sub>x</sub> emissions  
761 along a West Siberian natural gas pipeline, *npj Climate and Atmospheric Science*, 3(1),  
762 p.16, 2020.

763 Adams, C., McLinden, C. A., Shephard, M. W., Dickson, N., Dammers, E., Chen, J., Makar,  
764 P., Cady-Pereira, K. E., Tam, N., Kharol, S. K., Lamsal, L. N., and Krotkov, N. A.:  
765 Satellite-derived emissions of carbon monoxide, ammonia, and nitrogen dioxide from the  
766 2016 Horse River wildfire in the Fort McMurray area, *Atmos. Chem. Phys.*, 19, 2577–  
767 2599, <https://doi.org/10.5194/acp-19-2577-2019>, 2019.

768 Alvarado, M. J., Cady-Pereira, K. E., Xiao, Y., Millet, D. B., and Payne, V. H.: Emission Ratios  
769 for Ammonia and Formic Acid and Observations of Peroxy Acetyl Nitrate (PAN) and  
770 Ethylene in Biomass Burning Smoke as Seen by the Tropospheric Emission Spectrometer  
771 (TES), *Atmosphere*, 2, 633–654, doi:10.3390/atmos2040633, 2011.

772 Andela, N., Morton, D. C., Giglio, L., Chen, Y., Van Der Werf, G. R., Kasibhatla, P. S.,  
773 Defries, R. S., Collatz, G. J., Hantson, S., Kloster, S., Bachelet, D., Forrest, M., Lasslop,  
774 G., Li, F., Mangeon, S., Melton, J. R., Yue, C., and Randerson, J. T.: A human-driven



775 decline in global burned area, *Science*, 356, 1356–1362,  
776 <https://doi.org/10.1126/science.aal4108>, 2017.

777 Andela, N., Morton, D. C., Giglio, L., Paugam, R., Chen, Y., Hantson, S., van der Werf, G. R.,  
778 and Randerson, J. T.: The Global Fire Atlas of individual fire size, duration, speed and  
779 direction, *Earth Syst. Sci. Data*, 11, 529–552, <https://doi.org/10.5194/essd-11-529-2019>,  
780 2019.

781 Andela, N., Morton, D. C., Schroeder, W., Chen, Y., Brando, P. M. and Randerson, J. T.:  
782 Tracking and classifying Amazon fire events in near real time. *Science advances*, 8(30),  
783 p.eabd2713, <https://doi.org/10.1126/sciadv.abd2713>, 2022.

784 Andreae, M. O.: Emission of trace gases and aerosols from biomass burning – an updated  
785 assessment, *Atmos. Chem. Phys.*, 19, 8523–8546, [https://doi.org/10.5194/acp-19-8523-](https://doi.org/10.5194/acp-19-8523-2019)  
786 2019, 2019.

787 Apituley A., Pedernana, M., Sneep, M., Veeffkind, J. P., Loyola, D., Landgraf, J. and  
788 Borsdorff, T.: Sentinel-5 precursor/TROPOMI Level 2 Product User Manual Carbon  
789 Monoxide, Netherlands Institute for Space Research (SRON) report SRON-S5P-LEV2-  
790 MA-002,

791 [https://sentinel.esa.int/documents/247904/2474726/Sentinel-5P-Level-2-Product-User-](https://sentinel.esa.int/documents/247904/2474726/Sentinel-5P-Level-2-Product-User-Manual-Carbon-Monoxide.pdf/dc93c3ae-6c77-4673-8fe7-459635aba4a3)  
792 [Manual-Carbon-Monoxide.pdf/dc93c3ae-6c77-4673-8fe7-459635aba4a3](https://sentinel.esa.int/documents/247904/2474726/Sentinel-5P-Level-2-Product-User-Manual-Carbon-Monoxide.pdf/dc93c3ae-6c77-4673-8fe7-459635aba4a3), 2022.

793 Bauwens, M., Stavrou, T., Müller, J.-F., De Smedt, I., Van Roozendaal, M., van der Werf,  
794 G. R., Wiedinmyer, C., Kaiser, J. W., Sindelarova, K., and Guenther, A.: Nine years of  
795 global hydrocarbon emissions based on source inversion of OMI formaldehyde  
796 observations, *Atmos. Chem. Phys.*, 16, 10133–10158, [https://doi.org/10.5194/acp-16-](https://doi.org/10.5194/acp-16-10133-2016)  
797 10133-2016, 2016.



- 798 Boer, M. M., Resco de Dios, V., and Bradstock, R. A.: Unprecedented burn area of Australian  
799 mega forest fires, *Nat. Clim. Chang.* 10, 171–172, [https://doi.org/10.1038/s41558-020-](https://doi.org/10.1038/s41558-020-0716-1)  
800 0716-1, 2020.
- 801 Borsdorff, T., Hasekamp, O. P., Wassmann, A., and Landgraf, J.: Insights into Tikhonov  
802 regularization: application to trace gas column retrieval and the efficient calculation of total  
803 column averaging kernels, *Atmos. Meas. Tech.*, 7, 523–535, [https://doi.org/10.5194/amt-](https://doi.org/10.5194/amt-7-523-2014)  
804 7-523-2014, 2014.
- 805 Borsdorff, T., Aan de Brugh, J., Hu, H., Aben, I., Hasekamp, O., and Landgraf, J.: Measuring  
806 Carbon Monoxide With TROPOMI: First Results and a Comparison With ECMWF-IFS  
807 Analysis Data, *Geophys. Res. Lett.*, 45, 2826–2832,  
808 <https://doi.org/10.1002/2018GL077045>, 2018.
- 809 Bowman, D. M., Kolden, C. A., Abatzoglou, J. T., Johnston, F. H., van der Werf, G. R., and  
810 Flannigan, M.: Vegetation fires in the Anthropocene, *Nat. Rev. Earth Environ.*, 1, 500–515,  
811 <https://doi.org/10.1038/s43017-020-0085-3>, 2020.
- 812 Chuvieco, E., Mouillot, F., van der Werf, G. R., San Miguel, J., Tanasse, M., Koutsias, N.,  
813 García, M., Yebra, M., Padilla, M., Gitas, I., Heil, A., Hawbaker, T. J., and Giglio, L.:  
814 Historical background and current developments for mapping burned area from satellite  
815 Earth observation, *Remote Sensing of Environment*, 225, 45–64,  
816 <https://doi.org/10.1016/j.rse.2019.02.013>, 2019.
- 817 Chuvieco, E., Aguado, I., Salas, J., García, M., Yebra, M., and Oliva, P.: Satellite Remote  
818 Sensing Contributions to Wildland Fire Science and Management, *Curr Forestry Rep*,  
819 <https://doi.org/10.1007/s40725-020-00116-5>, 2020.
- 820



- 821 Castellanos, P., Boersma, K. F., and van der Werf, G. R.: Satellite observations indicate  
822 substantial spatiotemporal variability in biomass burning NO<sub>x</sub> emission factors for South  
823 America, *Atmos. Chem. Phys.*, 14, 3929–3943, <https://doi.org/10.5194/acp-14-3929-2014>,  
824 2014.
- 825 Ding, J., van der A, R. J., Mijling, B., and Levelt, P. F.: Space-based NO<sub>x</sub> emission estimates  
826 over remote regions improved in DECSO, *Atmos. Meas. Tech.*, 10, 925–938,  
827 <https://doi.org/10.5194/amt-10-925-2017>, 2017.
- 828 Douros, J., Eskes, H., van Geffen, J., Boersma, K. F., Compernelle, S., Pinardi, G.,  
829 Blechschmidt, A.-M., Peuch, V.-H., Colette, A., and Veefkind, P.: Comparing Sentinel-5P  
830 TROPOMI NO<sub>2</sub> column observations with the CAMS regional air quality ensemble,  
831 *Geosci. Model Dev.*, 16, 509–534, <https://doi.org/10.5194/gmd-16-509-2023>, 2023.
- 832 Eskes, H. J. and Eichmann K.-U.: S5P MPC Product Readme Nitrogen Dioxide, Report S5P-  
833 MPC-KNMI-PRF-NO<sub>2</sub>, version 2.1, ESA, [http://www.tropomi.eu/data-products/nitrogen-](http://www.tropomi.eu/data-products/nitrogen-dioxide/)  
834 [dioxide/](http://www.tropomi.eu/data-products/nitrogen-dioxide/) (last access: June 2023), 2021.
- 835 Eskes, H. J., van Geffen, J. H. G. M., Boersma, K. F., and Eichmann K.-U.. Apituley, A.,  
836 Pedergnana, M., Sneep, M., Veefkind, J. P., and Loyola, D.: S5P/TROPOMI Level-2  
837 Product User Manual Nitrogen Dioxide, Report S5P-KNMI-L2-0021-MA, version 4.0.2,  
838 ESA, [https://sentinel.esa.int/documents/247904/2474726/Sentinel-5P-Level-2-Product-](https://sentinel.esa.int/documents/247904/2474726/Sentinel-5P-Level-2-Product-User-Manual-Nitrogen-Dioxide.pdf)  
839 [User-Manual-Nitrogen-Dioxide.pdf](https://sentinel.esa.int/documents/247904/2474726/Sentinel-5P-Level-2-Product-User-Manual-Nitrogen-Dioxide.pdf) (last access: 7 March 2022), 2022.
- 840 Filkov, A. I., Ngo, T., Matthews, S., Telfer, S., and Penman, T. D.: Impact of Australia's  
841 catastrophic 2019/20 bushfire season on communities and environment. Retrospective  
842 analysis and current trends, *J. Safety Sci. Resilience*, 1, 44–56,  
843 <https://doi.org/10.1016/j.jnlssr.2020.06.009>, 2020.





- 844 Flemming, J., Huijnen, V., Arteta, J., Bechtold, P., Beljaars, A., Blechschmidt, A.-M.,  
845 Diamantakis, M., Engelen, R. J., Gaudel, A., Inness, A., Jones, L., Josse, B., Katragkou,  
846 E., Marecal, V., Peuch, V.-H., Richter, A., Schultz, M. G., Stein, O., and Tsikerdekis, A.:  
847 Tropospheric chemistry in the Integrated Forecasting System of ECMWF, *Geosci. Model*  
848 *Dev.*, 8, 975–1003, <https://doi.org/10.5194/gmd-8-975-2015>, 2015.
- 849 Finch, D. P., Palmer, P. I., and Zhang, T.: Automated detection of atmospheric NO<sub>2</sub> plumes  
850 from satellite data: a tool to help infer anthropogenic combustion emissions, *Atmos. Meas.*  
851 *Tech.*, 15, 721–733, <https://doi.org/10.5194/amt-15-721-2022>, 2022.
- 852 Gaubert, B., Emmons, L. K., Raeder, K., Tilmes, S., Miyazaki, K., Arellano Jr., A. F., Elguindi,  
853 N., Granier, C., Tang, W., Barré, J., Worden, H. M., Buchholz, R. R., Edwards, D. P.,  
854 Franke, P., Anderson, J. L., Saunio, M., Schroeder, J., Woo, J.-H., Simpson, I. J., Blake,  
855 D. R., Meinardi, S., Wennberg, P. O., Crouse, J., Teng, A., Kim, M., Dickerson, R. R.,  
856 He, H., Ren, X., Pusede, S. E., and Diskin, G. S.: Correcting model biases of CO in East  
857 Asia: impact on oxidant distributions during KORUS-AQ, *Atmos. Chem. Phys.*, 20,  
858 14617–14647, <https://doi.org/10.5194/acp-20-14617-2020>, 2020.
- 859 van Geffen, J., Boersma, K. F., Eskes, H., Sneep, M., ter Linden, M., Zara, M., and Veeffkind,  
860 J. P.: S5P TROPOMI NO<sub>2</sub> slant column retrieval: method, stability, uncertainties and  
861 comparisons with OMI, *Atmos. Meas. Tech.*, 13, 1315–1335, [https://doi.org/10.5194/amt-](https://doi.org/10.5194/amt-13-1315-2020)  
862 [13-1315-2020](https://doi.org/10.5194/amt-13-1315-2020), 2020.
- 863 van Geffen, J. H. G. M., Eskes, H. J., Boersma, K. F., and Veeffkind, J. P.: TROPOMI ATBD  
864 of the total and tropospheric NO<sub>2</sub> data products, Tech. Rep. S5P-KNMI-L2-0005-RP,  
865 Koninklijk Nederlands Meteorologisch Instituut (KNMI),  
866 <https://sentinels.copernicus.eu/documents/247904/2476257/Sentinel-5P-TROPOMI->



- 867 ATBD-NO2-data-products (last access: 22 January 2023), CI-7430-ATBD, issue 2.2.0, 16  
868 June 2021.
- 869 van Geffen, J., Eskes, H., Compernelle, S., Pinardi, G., Verhoelst, T., Lambert, J.-C., Sneep,  
870 M., ter Linden, M., Ludewig, A., Boersma, K. F., and Veefkind, J. P.: Sentinel-5P  
871 TROPOMI NO<sub>2</sub> retrieval: impact of version v2.2 improvements and comparisons with  
872 OMI and ground-based data, *Atmos. Meas. Tech.*, 15, 2037–2060,  
873 <https://doi.org/10.5194/amt-15-2037-2022>, 2022.
- 874 Goudar, M., Anema, J. C. S., Kumar, R., Borsdorff, T., and Landgraf, J.: Plume detection and  
875 emission estimate for biomass burning plumes from TROPOMI carbon monoxide  
876 observations using APE v1.1, *Geosci. Model Dev.*, 16, 4835–4852,  
877 <https://doi.org/10.5194/gmd-16-4835-2023>, 2023.
- 878 de Graaf, M.: Absorbing Aerosol Index: Sensitivity analysis, application to GOME and  
879 comparison with TOMS, *J. Geophys. Res.*, 110, 110,  
880 <https://doi.org/10.1029/2004JD005178>, 2005.
- 881 Griffin, D., McLinden, C. A., Dammers, E., Adams, C., Stockwell, C. E., Warneke, C.,  
882 Bourgeois, I., Peischl, J., Ryerson, T. B., Zarzana, K. J., Rowe, J. P., Volkamer, R., Knote,  
883 C., Kille, N., Koenig, T. K., Lee, C. F., Rollins, D., Rickly, P. S., Chen, J., Fehr, L.,  
884 Bourassa, A., Degenstein, D., Hayden, K., Mihele, C., Wren, S. N., Liggio, J., Akingunola,  
885 A., and Makar, P.: Biomass burning nitrogen dioxide emissions derived from space with  
886 TROPOMI: methodology and validation, *Atmos. Meas. Tech.*, 14, 7929–7957,  
887 <https://doi.org/10.5194/amt-14-7929-2021>, 2021.
- 888 Griffin, D., Chen, J., Anderson, K., Makar, P., McLinden, C. A., Dammers, E., and Fogal, A.:  
889 Towards an improved understanding of wildfire CO emissions: a satellite remote-sensing  
890 perspective, *EGUsphere [preprint]*, <https://doi.org/10.5194/egusphere-2023-649>, 2023.



- 891 Herman, J. R., Bhartia, P. K., Torres, O., Hsu, C., and Seftor, C.: Global distribution of UV-  
892 absorbing aerosols from Nimbus 7/TOMS data, *J. Geophys. Res.*, 102, 16911–16922, 1997
- 893 Higuera, P. E. and Abatzoglou, J. T.: Record-setting climate enabled the extraordinary 2020  
894 fire season in the western United States. *Global change biology*, 27(1),  
895 <https://doi.org/10.1111/gcb.15388>, 2021.
- 896 Hooghiemstra, P. B., Krol, M. C., Meirink, J. F., Bergamaschi, P., van der Werf, G. R., Novelli,  
897 P. C., Aben, I., and Röckmann, T.: Optimizing global CO emission estimates using a four-  
898 dimensional variational data assimilation system and surface network observations, *Atmos.*  
899 *Chem. Phys.*, 11, 4705–4723, <https://doi.org/10.5194/acp-11-4705-2011>, 2011.
- 900 Huijnen, V., Williams, J., van Weele, M., van Noije, T., Krol, M., Dentener, F., Segers, A.,  
901 Houweling, S., Peters, W., de Laat, J., Boersma, F., Bergamaschi, P., van Velthoven, P.,  
902 Le Sager, P., Eskes, H., Alkemade, F., Scheele, R., Nédélec, P., and Pätz, H.-W.: The global  
903 chemistry transport model TM5: description and evaluation of the tropospheric chemistry  
904 version 3.0, *Geosci. Model Dev.*, 3, 445–473, <https://doi.org/10.5194/gmd-3-445-2010>,  
905 2010.
- 906 Huijnen, V., Wooster, M. J., Kaiser, J. W., Gaveau, D. L. A., Flemming, J., Parrington, M.,  
907 Inness, A., Murdiyoso, D., Main, B., and van Weele, M.: Fire carbon emissions over  
908 maritime southeast Asia in 2015 largest since 1997, *Sci. Rep.-UK*, 6, 26886,  
909 <https://doi.org/10.1038/srep26886>, 2016.
- 910 Huijnen, V., Pozzer, A., Arteta, J., Brasseur, G., Bouarar, I., Chabrillat, S., Christophe, Y.,  
911 Doumbia, T., Flemming, J., Guth, J., Josse, B., Karydis, V. A., Marecal, V. and S. Pelletier  
912 : Quantifying uncertainties due to chemistry modelling – evaluation of tropospheric  
913 composition simulations in the cams model (cycle 43r1). *Geosci. Model Dev.*, 12, 1725–  
914 1752, 2019.



- 915 Inness, A., Aben, I., Ades, M., Borsdorff, T., Flemming, J., Jones, L., Landgraf, J., Langerock,  
916 B., Nedelec, P., Parrington, M., and Ribas, R.: Assimilation of S5P/TROPOMI carbon  
917 monoxide data with the global CAMS near-real-time system, *Atmos. Chem. Phys.*, 22,  
918 14355–14376, <https://doi.org/10.5194/acp-22-14355-2022>, 2022.
- 919 Jin, X., Zhu, Q., and Cohen, R. C.: Direct estimates of biomass burning NO<sub>x</sub> emissions and  
920 lifetimes using daily observations from TROPOMI, *Atmos. Chem. Phys.*, 21, 15569–  
921 15587, <https://doi.org/10.5194/acp-21-15569-2021>, 2021.
- 922 Kaiser, J. W., Heil, A., Andreae, M. O., Benedetti, A., Chubarova, N., Jones, L., Morcrette, J.-  
923 J., Razinger, M., Schultz, M. G., Suttie, M., and van der Werf, G. R.: Biomass burning  
924 emissions estimated with a global fire assimilation system based on observed fire radiative  
925 power, *Biogeosciences*, 9, 527–554, <https://doi.org/10.5194/bg-9-527-2012>, 2012.
- 926 Khaldi, R., Alcaraz-Segura, D., Guirado, E., Benhammou, Y., El Afia, A., Herrera, F., and  
927 Tabik, S.: TimeSpec4LULC: a global multispectral time series database for training LULC  
928 mapping models with machine learning, *Earth Syst. Sci. Data*, 14, 1377–1411,  
929 <https://doi.org/10.5194/essd-14-1377-2022>, 2022.
- 930 Konovalov, I. B., Berezin, E. V., Ciais, P., Broquet, G., Beekmann, M., Hadji-Lazaro, J.,  
931 Clerbaux, C., Andreae, M. O., Kaiser, J. W., and Schulze, E.-D.: Constraining CO<sub>2</sub>  
932 emissions from open biomass burning by satellite observations of co-emitted species: a  
933 method and its application to wildfires in Siberia, *Atmos. Chem. Phys.*, 14, 10383–10410,  
934 <https://doi.org/10.5194/acp-14-10383-2014>, 2014.
- 935 Krol, M., Houweling, S., Bregman, B., van den Broek, M., Segers, A., van Velthoven, P.,  
936 Peters, W., Dentener, F., and Bergamaschi, P.: The two-way nested global chemistry-  
937 transport zoom model TM5: algorithm and applications, *Atmos. Chem. Phys.*, 5, 417–432,  
938 <https://doi.org/10.5194/acp-5-417-2005>, 2005.



- 939 Kurchuba, S, van Vliet, J., Verbeek, F. J., Meulman, J. J., and Veenman, C. J.: "Supervised  
940 Segmentation of NO<sub>2</sub> Plumes from Individual Ships Using TROPOMI Satellite Data",  
941 Remote Sensing 14, no. 22: 5809. <https://doi.org/10.3390/rs14225809>, 2022.
- 942 Lambert, J.-C., Keppens, A., Compernelle, S., Eichmann, K.-U., de Graaf, M., Hubert, DB.  
943 Langerock, B., Ludewig, A., Sha, M.K., Verhoelst, T., Wagner, T, Ahn, C., Argyrouli, A.,  
944 Balis, D., Chan, K. L., Coldewey-Egbers, M., De Smedt, I., Eskes, H., Fjæraa, A. M.,  
945 Garane, K., Gleason, J. F., Goutail, F., Granville, J., Hedelt, P., Ahn, C., Heue, K.-P.,  
946 Jaross, G., Kleipool, QML. Koukouli, M. LR. Lutz, R., Martinez Velarte, M. C,  
947 Michailidis, K., Nanda, S., Niemeijer, S Pazmiño, A., Pinardi, G., Richter, A., Rozemeijer,  
948 N., Sneep, M., Stein Zweers, D., Theys, N. Tilstra, G., Torres, O., Valks, P., van Geffen,  
949 J., Vigouroux, C., Wang, P., and Weber, M.: Quarterly Validation Report of the Copernicus  
950 Sentinel-5 Precursor Operational Data Products #19: April 2018 – May 2023, S5P MPC  
951 Routine Operations Consolidated Validation Report series, Issue #19, Version 19.01.00,  
952 196 pp., 3 July 2023. Available at <https://mpc-vdaf.tropomi.eu/>
- 953 Lasslop, G., Coppola, A. I., Voulgarakis, A., Yue, C., and Veraverbeke, S.: Influence of Fire  
954 on the Carbon Cycle and Climate, Current Climate Change Reports, 5, 112–123,  
955 <https://doi.org/10.1007/s40641-019-00128-9>, 2019.
- 956 Lamsal, L. N., Martin, R. V., Padmanabhan, A., van Donkelaar, A., Zhang, Q., Sioris, C. E.,  
957 Chance, K., Kurosu, T. P., and Newchurch, M. J.: Application of satellite observations for  
958 timely updates to global anthropogenic NO<sub>x</sub> emission inventories, Geophys. Res. Lett., 38,  
959 L05810, <https://doi.org/10.1029/2010GL046476>, 2011.
- 960 Landgraf, J., aan de Brugh, J., Scheepmaker, R., Borsdorff, T., Hu, H., Houweling, S., Butz,  
961 A., Aben, I., and Hasekamp, O.: Carbon monoxide total column retrievals from TROPOMI



962 shortwave infrared measurements, *Atmos. Meas. Tech.*, 9, 4955–4975,  
963 <https://doi.org/10.5194/amt-9-4955-2016>, 2016.

964 Landgraf, J., aan de Brugh, J., Scheepmaker, R., Borsdorff, T. Houweling, S. and Hasekamp,  
965 O.: Algorithm Theoretical Baseline Document for Sentinel-5 Precursor: Carbon Monoxide  
966 Total Column Retrieval, Netherlands Institute for Space Research (SRON) report SRON-  
967 S5P-LEV2-RP-002, [https://sentinel.esa.int/documents/247904/2476257/Sentinel-5P-](https://sentinel.esa.int/documents/247904/2476257/Sentinel-5P-TROPOMI-ATBD-Carbon-Monoxide-Total-Column-Retrieval.pdf)  
968 [TROPOMI-ATBD-Carbon-Monoxide-Total-Column-Retrieval.pdf](https://sentinel.esa.int/documents/247904/2476257/Sentinel-5P-TROPOMI-ATBD-Carbon-Monoxide-Total-Column-Retrieval.pdf), 2022a.

969 Landgraf, J., Borsdorff, T., Langerock, B., and Keppens, A., S5P MPC Product Readme  
970 Carbon Monoxide, Report S5P-MPC-SRON-PRF-CO, version 2.5,  
971 [https://sentinels.copernicus.eu/web/sentinel/user-guides/sentinel-5p-tropomi/document-](https://sentinels.copernicus.eu/web/sentinel/user-guides/sentinel-5p-tropomi/document-library/-/asset_publisher/w9Mnd6VPjXlc/content/sentinel-5p-tropomi-carbon-monoxide-total-column-retrieval-atbd)  
972 [library/-/asset\\_publisher/w9Mnd6VPjXlc/content/sentinel-5p-tropomi-carbon-monoxide-](https://sentinels.copernicus.eu/web/sentinel/user-guides/sentinel-5p-tropomi/document-library/-/asset_publisher/w9Mnd6VPjXlc/content/sentinel-5p-tropomi-carbon-monoxide-total-column-retrieval-atbd)  
973 [total-column-retrieval-atbd](https://sentinels.copernicus.eu/web/sentinel/user-guides/sentinel-5p-tropomi/document-library/-/asset_publisher/w9Mnd6VPjXlc/content/sentinel-5p-tropomi-carbon-monoxide-total-column-retrieval-atbd), 2022b.

974 Lee, J. H., Lee, S. H. and Kim, H. C.: Detection of strong NOX emissions from fine-scale  
975 reconstruction of the OMI tropospheric NO2 product. *Remote Sensing*, 11(16), p.1861,  
976 <https://doi.org/10.3390/rs11161861>, 2019.

977 Li, F., Zhang, X., Kondragunta, S., and Lu, X.: An evaluation of advanced baseline imager fire  
978 radiative power based wildfire emissions using carbon monoxide observed by the  
979 Tropospheric Monitoring Instrument across the conterminous United States, *Environ. Res.*  
980 *Let.*, 15, 094049, <https://doi.org/10.1088/1748-9326/ab9d3a>, 2020.

981 Lin, C., Cohen, J. B., Wang, S., and Lan, R.: Application of a combined standard deviation and  
982 mean based approach to MOPITT CO column data, and resulting improved representation  
983 of biomass burning and urban air pollution sources, *Remote Sensing of Environment*, 241,  
984 111720. <https://doi.org/10.1016/j.rse.2020.111720>, 2020.



- 985 Liu, L., Zhang, X., Gao, Y., Chen, X., Shuai, X., and Mi, J.: Finer-Resolution Mapping of  
986 Global Land Cover: Recent Developments, Consistency Analysis, and Prospects, *J. Remote*  
987 *Sens.*, 2021, 1–38, 2021.
- 988 Martínez-Alonso, S., Deeter, M., Worden, H., Borsdorff, T., Aben, I., Commane, R., Daube,  
989 B., Francis, G., George, M., Landgraf, J., Mao, D., McKain, K., and Wofsy, S.: 1.5 years  
990 of TROPOMI CO measurements: comparisons to MOPITT and ATom, *Atmos. Meas.*  
991 *Tech.*, 13, 4841–4864, <https://doi.org/10.5194/amt-13-4841-2020>, 2020.
- 992 McLauchlan, K. K., Higuera, P. E., Miesel, J., Rogers, B. M., Schweitzer, J., Shuman, J. K.,  
993 Tepley, A. J., Varner, J. M., Veblen, T. T., Adalsteinsson, S. A., and Balch, J. K.: Fire as a  
994 fundamental ecological process: Research advances and frontiers. *J. Ecol.*, 108 (5), 2047-  
995 2069, <https://doi.org/10.1111/1365-2745.13403>, 2019.
- 996 Mebust, A. K., Russell, A. R., Hudman, R. C., Valin, L. C., and Cohen, R. C.: Characterization  
997 of wildfire NO<sub>x</sub> emissions using MODIS fire radiative power and OMI tropospheric NO<sub>2</sub>  
998 columns, *Atmos. Chem. Phys.*, 11, 5839–5851, <https://doi.org/10.5194/acp-11-5839-2011>,  
999 2011.
- 1000 Mebust, A. K. and Cohen, R. C.: Observations of a seasonal cycle in NO<sub>x</sub> emissions from fires  
1001 in African woody savannas, *Geophys. Res. Lett.*, 40, 1451–1455,  
1002 <https://doi.org/10.1002/grl.50343>, 2013.
- 1003 Mebust, A. K. and Cohen, R. C.: Space-based observations of fire NO<sub>x</sub> emission coefficients:  
1004 a global biome-scale comparison, *Atmos. Chem. Phys.*, 14, 2509–2524,  
1005 <https://doi.org/10.5194/acp-14-2509-2014>, 2014.
- 1006 Mijling, B., van der A, R. J., and Zhang, Q.: Regional nitrogen oxides emission trends in East  
1007 Asia observed from space, *Atmos. Chem. Phys.*, 13, 12003–12012,  
1008 <https://doi.org/10.5194/acp-13-12003-2013>, 2013.



- 1009 Peiro, H., Crowell, S., and Moore III, B.: Optimizing 4 years of CO<sub>2</sub> biospheric fluxes from  
1010 OCO-2 and in situ data in TM5: fire emissions from GFED and inferred from MOPITT CO  
1011 data, *Atmos. Chem. Phys.*, 22, 15817–15849, <https://doi.org/10.5194/acp-22-15817-2022>,  
1012 2022
- 1013 Penning de Vries, M. J. M., Beirle, S., and Wagner, T.: UV Aerosol Indices from  
1014 SCIAMACHY: introducing the SCattering Index (SCI), *Atmos. Chem. Phys.*, 9, 9555–  
1015 9567, <https://doi.org/10.5194/acp-9-9555-2009>, 2009.
- 1016 Petrenko, M., Kahn, R., Chin, M., Soja, A., and Kucsera, T.: The use of satellite-measured  
1017 aerosol optical depth to constrain biomass burning emissions source strength in the global  
1018 model GOCART, *J. Geophys. Res.-Atmos.*, 117, D18212,  
1019 <https://doi.org/10.1029/2012JD017870>, 2012.
- 1020 Rémy, S., Kipling, Z., Huijnen, V., Flemming, J., Nabat, P., Michou, M., Ades, M., Engelen,  
1021 R., and Peuch, V.-H.: Description and evaluation of the tropospheric aerosol scheme in the  
1022 Integrated Forecasting System (IFS-AER, cycle 47R1) of ECMWF, *Geosci. Model Dev.*,  
1023 15, 4881–4912, <https://doi.org/10.5194/gmd-15-4881-2022>, 2022.
- 1024 Sandu, A. and Sander, R.: Technical note: Simulating chemical systems in Fortran90 and  
1025 Matlab with the Kinetic PreProcessor KPP-2.1, *Atmos. Chem. Phys.*, 6, 187–195,  
1026 <https://doi.org/10.5194/acp-6-187-2006>, 2006.
- 1027 Schneising, O., Buchwitz, M., Reuter, M., Bovensmann, H., Burrows, J. P., Borsdorff, T.,  
1028 Deutscher, N. M., Feist, D. G., Griffith, D. W. T., Hase, F., Hermans, C., Iraci, L. T., Kivi,  
1029 R., Landgraf, J., Morino, I., Notholt, J., Petri, C., Pollard, D. F., Roche, S., Shiomi, K.,  
1030 Strong, K., Sussmann, R., Velazco, V. A., Warneke, T., and Wunch, D.: A scientific  
1031 algorithm to simultaneously retrieve carbon monoxide and methane from TROPOMI





- 1032 onboard Sentinel-5 Precursor, *Atmos. Meas. Tech.*, 12, 6771–6802,  
1033 <https://doi.org/10.5194/amt-12-6771-2019>, 2019.
- 1034 Schreier, S. F., Richter, A., Kaiser, J. W., and Burrows, J. P.: The empirical relationship  
1035 between satellite-derived tropospheric NO<sub>2</sub> and fire radiative power and possible  
1036 implications for fire emission rates of NO<sub>x</sub>, *Atmos. Chem. Phys.*, 14, 2447–2466,  
1037 <https://doi.org/10.5194/acp-14-2447-2014>, 2014.
- 1038 Schuit, B. J., Maasackers, J. D., Bijl, P., Mahapatra, G., van den Berg, A.-W., Pandey, S.,  
1039 Lorente, A., Borsdorff, T., Houweling, S., Varon, D. J., McKeever, J., Jervis, D., Girard,  
1040 M., Irakulis-Loitxate, I., Gorroño, J., Guanter, L., Cusworth, D. H., and Aben, I.:  
1041 Automated detection and monitoring of methane super-emitters using satellite data, *Atmos.*  
1042 *Chem. Phys.*, 23, 9071–9098, <https://doi.org/10.5194/acp-23-9071-2023>, 2023.
- 1043 Sha, M. K., Langerock, B., Blavier, J.-F. L., Blumenstock, T., Borsdorff, T., Buschmann, M.,  
1044 Dehn, A., De Mazière, M., Deutscher, N. M., Feist, D. G., García, O. E., Griffith, D. W.  
1045 T., Grutter, M., Hannigan, J. W., Hase, F., Heikkinen, P., Hermans, C., Iraci, L. T., Jeseck,  
1046 P., Jones, N., Kivi, R., Kumps, N., Landgraf, J., Lorente, A., Mahieu, E., Makarova, M. V.,  
1047 Mellqvist, J., Metzger, J.-M., Morino, I., Nagahama, T., Notholt, J., Ohyama, H., Ortega,  
1048 I., Palm, M., Petri, C., Pollard, D. F., Rettinger, M., Robinson, J., Roche, S., Roehl, C. M.,  
1049 Röhling, A. N., Rousogonous, C., Schneider, M., Shiomi, K., Smale, D., Stremme, W.,  
1050 Strong, K., Sussmann, R., Té, Y., Uchino, O., Velazco, V. A., Vigouroux, C., Vrekoussis,  
1051 M., Wang, P., Warneke, T., Wizenberg, T., Wunch, D., Yamanouchi, S., Yang, Y., and  
1052 Zhou, M.: Validation of methane and carbon monoxide from Sentinel-5 Precursor using  
1053 TCCON and NDACC-IRWG stations, *Atmos. Meas. Tech.*, 14, 6249–6304,  
1054 <https://doi.org/10.5194/amt-14-6249-2021>, 2021.



- 1055 Sitnov, S. A. and Mokhov, I. I.: Formaldehyde and nitrogen dioxide in the atmosphere during  
1056 summer weather extremes and wildfires in European Russia in 2010 and Western Siberia  
1057 in 2012. *International Journal of Remote Sensing*, 38(14), pp.4086-4106,  
1058 <https://doi.org/10.1080/01431161.2017.1312618> , 2017.
- 1059 Soulie, A.; Granier, C.; Darras, S.; Doumbia, T.; Guevara, M.; Jalkanen, J.P.; Keita, S.;  
1060 Liousse, C.; Crippa, M.; Guizzardi, D.; et al. Global anthropogenic emissions (CAM5-  
1061 GLOB-ANT) for the copernicus atmosphere monitoring service air quality forecasting and  
1062 reanalyses. *Earth System Science Data discussion*, 2023.
- 1063 Stavrakou, T., Müller, J.-F., Bauwens, M., De Smedt, I., Van Roozendael, M., De Mazière, M.,  
1064 Vigouroux, C., Hendrick, F., George, M., Clerbaux, C., Coheur, P.-F., and Guenther, A.:  
1065 How consistent are top-down hydrocarbon emissions based on formaldehyde observations  
1066 from GOME-2 and OMI?, *Atmos. Chem. Phys.*, 15, 11861–11884,  
1067 <https://doi.org/10.5194/acp-15-11861-2015>, 2015.
- 1068 Stein Zweers, D. C.: TROPOMI ATBD of the UV aerosol index, Technical Report S5P-KNMI-  
1069 L2-0008-RP, Koninklijk Nederlands Meteorologisch Instituut (KNMI),  
1070 [https://sentinel.esa.int/documents/247904/2476257/Sentinel-5P-TROPOMI-ATBD-UV-](https://sentinel.esa.int/documents/247904/2476257/Sentinel-5P-TROPOMI-ATBD-UV-Aerosol-Index.pdf)  
1071 [Aerosol-Index.pdf](https://sentinel.esa.int/documents/247904/2476257/Sentinel-5P-TROPOMI-ATBD-UV-Aerosol-Index.pdf), 2016.
- 1072 Stockwell, C. E., Bela, M. M., Coggon, M. M., Gkatzelis, G. I., Wiggins, E., Gargulinski, E.  
1073 M., Shingler, T., Fenn, M., Griffin, D., Holmes, C. D., Ye, X., Saide, P. E., Bourgeois, I.,  
1074 Peischl, J., Womack, C. C., Washenfelder, R. A., Veres, P. R., Neuman, J. A., Gilman, J.  
1075 B., Lamplugh, A., Schwantes, R. H., McKeen, S. A., Wisthaler, A., Piel, F., Guo, H.,  
1076 Campuzano-Jost, P., Jimenez, J. L., Fried, A., Hanisco, T. F., Huey, L. G., Perring, A.,  
1077 Katich, J. M., Diskin, G. S., Nowak, J. B., Bui, T. P., Halliday, H. S., DiGangi, J. P., Pereira,  
1078 G., James, E. P., Ahmadov, R., McLinden, C. A., Soja, A. J., Moore, R. H., Hair, J. W.,



- 1079 and Warneke, C.: Airborne emission rate measurements validate remote sensing  
1080 observations and emission inventories of western U.S. wildfires, *Environ. Sci. Technol.*,  
1081 56, 7564–7577, <https://doi.org/10.1021/acs.est.1c07121>, 2022.
- 1082 Tanimoto, H., Ikeda, K., Folkert Boersma, K., Van Der A, R. J., and Garivait, S.: Interannual  
1083 variability of nitrogen oxides emissions from boreal fires in Siberia and Alaska during  
1084 1996–2011 as observed from space, *Environ. Res. Lett.*, 10, 065004,  
1085 <https://doi.org/10.1088/1748-9326/10/6/065004>, 2015.
- 1086 Torres, O., Bhartia, P. K., Herman, J. R., and Ahmad, Z.: Derivation of aerosol properties from  
1087 satellite measurements of backscattered ultraviolet radiation: Theoretical basis, *J. Geophys.*  
1088 *Res.*, 103, 17099–17110, 1998.
- 1089 van der Velde, I. R., van der Werf, G. R., Houweling, S., Eskes, H. J., Veeffkind, J. P.,  
1090 Borsdorff, T., and Aben, I.: Biomass burning combustion efficiency observed from space  
1091 using measurements of CO and NO<sub>2</sub> by the TROPOspheric Monitoring Instrument  
1092 (TROPOMI), *Atmos. Chem. Phys.*, 21, 597–616, [https://doi.org/10.5194/acp-21-597-](https://doi.org/10.5194/acp-21-597-2021)  
1093 2021, 2021.
- 1094 Veeffkind, J. P., Aben, I., McMullan, K., Förster, H., de Vries, J., Otter, G., Claas, J., Eskes, H.  
1095 J., de Haan, J. F., Kleipool, Q., van Weele, M., Hasekamp, O., Hoogeveen, R., Landgraf,  
1096 J., Snel, R., Tol, P., Ingmann, P., Voors, R., Kruizinga, B., Vink, R., Visser, H., and Levelt,  
1097 P. F.: TROPOMI on the ESA Sentinel-5 Precursor: A GMES mission for global  
1098 observations of the atmospheric composition for climate, air quality and ozone layer  
1099 applications, *Remote Sens. Environ.*, 120, 70–83,  
1100 <https://doi.org/10.1016/j.rse.2011.09.027>, 2012.
- 1101 Verhoelst, T., Compernelle, S., Pinardi, G., Lambert, J.-C., Eskes, H. J., Eichmann, K.-U.,  
1102 Fjærraa, A. M., Granville, J., Niemeijer, S., Cede, A., Tiefengraber, M., Hendrick, F.,



- 1103 Pazmiño, A., Bais, A., Bazureau, A., Boersma, K. F., Bognar, K., Dehn, A., Donner, S.,  
1104 Elokhov, A., Gebetsberger, M., Goutail, F., Grutter de la Mora, M., Gruzdev, A., Gratsea,  
1105 M., Hansen, G. H., Irie, H., Jepsen, N., Kanaya, Y., Karagkiozidis, D., Kivi, R., Kreher,  
1106 K., Levelt, P. F., Liu, C., Müller, M., Navarro Comas, M., Peters, A. J. M., Pommereau, J.-  
1107 P., Portafaix, T., Prados-Roman, C., Puenteadura, O., Querel, R., Remmers, J., Richter, A.,  
1108 Rimmer, J., Rivera Cárdenas, C., Saavedra de Miguel, L., Sinyakov, V. P., Stremme, W.,  
1109 Strong, K., Van Roozendaal, M., Veefkind, J. P., Wagner, T., Wittrock, F., Yela González,  
1110 M., and Zehner, C.: Ground-based validation of the Copernicus Sentinel-5P TROPOMI  
1111 NO<sub>2</sub> measurements with the NDACC ZSL-DOAS, MAX-DOAS and Pandonia global  
1112 networks, *Atmos. Meas. Tech.*, 14, 481–510, <https://doi.org/10.5194/amt-14-481-2021>,  
1113 2021.
- 1114 Vidot, J., Landgraf, J., Hasekamp, O., Butz, A., Galli, A., Tol, P., and Aben, I.: Carbon  
1115 monoxide from shortwave infrared reflectance measurements: A new retrieval approach  
1116 for clear sky and partially cloudy atmospheres, *Remote Sens. Environ.*, 120, 255–266,  
1117 <https://doi.org/10.1016/j.rse.2011.09.032>, 2012.
- 1118 Wan, N., Xiong, X., Kluitenberg, G. J., Hutchinson, J. M. S., Aiken, R., Zhao, H., and Lin, X.:  
1119 Estimation of biomass burning emission of NO<sub>2</sub> and CO from 2019–2020 Australia fires  
1120 based on satellite observations, *Atmos. Chem. Phys.*, 23, 711–724,  
1121 <https://doi.org/10.5194/acp-23-711-2023>, 2023.
- 1122 van Wees, D., van der Werf, G. R., Randerson, J. T., Rogers, B. M., Chen, Y., Veraverbeke,  
1123 S., Giglio, L., and Morton, D. C.: Global biomass burning fuel consumption and emissions  
1124 at 500 m spatial resolution based on the Global Fire Emissions Database (GFED), *Geosci.*  
1125 *Model Dev.*, 15, 8411–8437, <https://doi.org/10.5194/gmd-15-8411-2022>, 2022.



- 1126 Whitburn, S., Van Damme, M., Kaiser, J. W., van der Werf, G. R., Turquety, S., Hurtmans, D.,  
1127 Clarisse, L., Clerbaux, C., and Coheur, P. F.: Ammonia emissions in tropical biomass  
1128 burning regions: Comparison between satellite-derived emissions and bottom-up fire  
1129 inventories, *Atmos. Environ.*, 121, 42–54, <https://doi.org/10.1016/j.atmosenv.2015.03.015>,  
1130 2015.
- 1131 Williams, J. E., Landgraf, J., Bregman, A., and Walter, H. H.: A modified band approach for  
1132 the accurate calculation of online photolysis rates in stratospheric-tropospheric Chemical  
1133 Transport Models, *Atmos. Chem. Phys.*, 6, 4137–4161, [https://doi.org/10.5194/acp-6-](https://doi.org/10.5194/acp-6-4137-2006)  
1134 4137-2006, 2006.
- 1135 Williams, J. E., van Velthoven, P. F. J., and Brenninkmeijer, C. A. M.: Quantifying the  
1136 uncertainty in simulating global tropospheric composition due to the variability in global  
1137 emission estimates of Biogenic Volatile Organic Compounds, *Atmos. Chem. Phys.*, 13,  
1138 2857–2891, <https://doi.org/10.5194/acp-13-2857-2013>, 2013.
- 1139 Williams, J. E., Huijnen, V., Bouarar, I., Meziane, M., Schreurs, T., Pelletier, S., Marécal, V.,  
1140 Josse, B., and Flemming, J.: Regional evaluation of the performance of the global CAMS  
1141 chemical modeling system over the United States (IFS cycle 47r1), *Geosci. Model Dev.*,  
1142 15, 4657–4687, <https://doi.org/10.5194/gmd-15-4657-2022>, 2022.
- 1143 Wooster, M. J., Roberts, G. J., Giglio, L., Roy, D. P., Freeborn, P. H., Boschetti, L., Justice,  
1144 C., Ichoku, C., Schroeder, W., Davies, D., Smith, A. M. S., Setzer, A., Csiszar, I., Strydom,  
1145 T., Frost, P., Zhang, T., Xu, W., de Jong, M. C., Johnston, J. M., Ellison, L., Vadrevu, K.,  
1146 Sparks, A. M., Nguyen, H., McCarty, J., Tanpipat, V., Schmidt, C., and San-Miguel-Ayanz,  
1147 J.: Satellite remote sensing of active fires: History and current status, applications and  
1148 future requirements, *Remote Sensing of Environment*, 267, 112694,  
1149 <https://doi.org/10.1016/j.rse.2021.112694>, 2021.



1150 Yin, Y., Chevallier, F., Ciais, P., Broquet, G., Fortems-Cheiney, A., Pison, I., and Saunois, M.:  
1151 Decadal trends in global CO emissions as seen by MOPITT, *Atmos. Chem. Phys.*, 15,  
1152 13433–13451, <https://doi.org/10.5194/acp-15-13433-2015>, 2015.

1153 Young, E. and Paton-Walsh, C.: Emission Ratios of the Tropospheric Ozone Precursors  
1154 Nitrogen Dioxide and Formaldehyde from Australia’s Black Saturday Fires, *Atmosphere*,  
1155 2, 617–632, 2011.

1156

## 1157 **Appendix**

1158

### 1159 **Application of Sentinel-5p TROPOMI data for fire monitoring**

1160 The launch of the Polar orbiting TROPOMI instrument on board of the Sentinel-5p (S5p)  
1161 satellite in October 2017 with at that time unprecedented spatial resolution, data accuracy and  
1162 precision has opened up a whole new range of possibilities for monitoring and studying fires.  
1163 Several research papers have been published in recent years exploring the use of TROPOMI  
1164 data for those particular applications.

1165 Li et al. (2020) used TROPOMI CO data for a selection of 41 wildfires across the United  
1166 States for a 15-month period in 2018-2019 to assess geostationary GOES-R FRP-based fire  
1167 emissions. CO emissions from TROPOMI data were estimated using a CO column mass budget  
1168 approach. They found a very good agreement between emissions based on both methods for  
1169 this selection of US wildfires.

1170 Van der Velde et al. (2021) presented a first analysis of daily TROPOMI NO<sub>2</sub>/CO ratios  
1171 uncovering spatio-temporal differences “that point to distinct differences in biomass burning  
1172 behavior”. Although they used daily (single fire) TROPOMI data they extracted data on



1173 regional to continental scale regions to derive statistical relationships. Using chemistry-  
1174 transport model simulations and bottom-up GFEDv4 fire emissions they found the model  
1175 results to be broadly consistent with the TROPOMI observations.

1176 Griffin et al. (2021) focused on a few selected North American fires in TROPOMI data to  
1177 estimate fire NO<sub>x</sub> emissions using plume model simulations while also comparing with *in situ*  
1178 field campaign data from the FIREX-AQ campaign. They found that there is a good agreement  
1179 between satellite observation and *in situ* data and that TROPOMI NO<sub>2</sub> data can be used to  
1180 determine single fire NO<sub>x</sub> emissions.

1181 Jin et al. (2021) calculated vegetation-specific NO<sub>x</sub> emissions and FRP emission factors  
1182 based on a large selection of isolated single fire emission plumes using TROPOMI and  
1183 Gaussian plume modelling. They found significant differences between previously reported  
1184 and observed emission factors suggesting a much larger variability amongst different fires than  
1185 generally assumed.

1186 Stockwell et al. (2022) used aircraft data to estimate fire emissions for five different fires  
1187 and compared them with geostationary observations of FRP and burned area as well as  
1188 emissions of carbon monoxide based on TROPOMI data. They found a strong correlation  
1189 between the emissions based on the *in-situ* data and the emissions based on the TROPOMI  
1190 data.

1191 Griffin et al. (2023) use TROPOMI CO data to create a global database of single or local  
1192 fire burning CO emissions for the period 2019-2021 to avoid smoke and cloud obscuring  
1193 effects of FRP measured by satellite instruments like MODIS and VIIRS. In addition, they also  
1194 use TROPOMI CO data to derive emission factors (“emission coefficients”), *i.e.* the amount of  
1195 CO emission as a function of FRP. They find a large range of biome dependent emission factors



1196 for different types of forests and conclude that simple biomes classifications for estimating fire  
1197 emissions are insufficient and that, if anything, further biomes distinction and refinement is  
1198 warranted. They also note that more information on the burning stage of a fire and temporal  
1199 fire development is crucial for improving fire emission estimates, which with the use of polar  
1200 orbiting satellite instruments is hampered by the once or twice per day overpass.

1201 Wan et al. (2023) analyzed TROPOMI NO<sub>2</sub> and CO data for the massive Australian 2020  
1202 “New Year’s bushfire event” with a focus on deriving emission ratios and emission factors for  
1203 different vegetation types. They note that TROPOMI data can help identify the relative  
1204 contributions of different flaming phases over larger regions.

1205 All these studies highlight the potential of using TROPOMI data for assessing fire  
1206 emissions. They also all note that their studies are the first exploratory steps using TROPOMI  
1207 and that more research is needed and warranted while approaches could be expanded, extended  
1208 and refined.

1209 The S4F project explores the suite of the Sentinel satellites using a novel synergetic  
1210 approach to derived global fire emissions based on the characterization of individual fires and  
1211 their behavior, eventually to better constrain total carbon emissions and emission factors. The  
1212 ESA Sentinels have a huge potential to observe and quantify fire dynamics in terms of pre-fire  
1213 surface conditions (vegetation cover and fuel moisture content), fire behavior (FRP, burned  
1214 area, fire size) and fire effects on the atmosphere (fire emissions of trace gases and aerosols).  
1215 However, this combined potential has not yet been exploited even though there is a clear need  
1216 for such an integrated synergetic approach.

1217





1218

1219 **IFS COMPO**

1220 The default tropospheric chemistry of IFS-COMPO as used here is based on CY48R1 as  
1221 described in [https://www.ecmwf.int/en/elibrary/81374-ifs-documentation-cy48r1-part-viii-](https://www.ecmwf.int/en/elibrary/81374-ifs-documentation-cy48r1-part-viii-atmospheric-composition)  
1222 [atmospheric-composition](https://www.ecmwf.int/en/elibrary/81374-ifs-documentation-cy48r1-part-viii-atmospheric-composition). Organic chemistry for trace gases up to propane is modeled  
1223 explicitly, while lumped tracers are used for specific types of functional groups to model the  
1224 oxidation of higher volatile organic compounds (Huijnen et al., 2010; Williams et al., 2013).  
1225 The updated isoprene oxidation parameterization is documented in Williams et al. (2022).  
1226 Photolysis rates in the troposphere are computed using the modified band approach (MBA)  
1227 (Williams et al., 2006, 2012). The tropospheric chemistry mechanism consists of 71 trace gases  
1228 and 127 gas-phase reactions, 30 photolysis rates, 3 heterogeneous reactions and 2 aqueous  
1229 phase reactions. It is solved based on Kinetic PreProcessor (KPP) routines, using the four stages  
1230 and third-order Rosenbrock solver (Sandu and Sander, 2006).

1231 The aerosol component in IFS-COMPO is described in Rémy et al. (2022) and is based on  
1232 a bulk-bin aerosol scheme. It simulates mass mixing ratio of the tracers for sea salt, desert dust,  
1233 organic matter (OM), black carbon (BC), sulfate, nitrate, ammonium, and secondary organic  
1234 aerosol (SOA), and is coupled to the tropospheric chemistry scheme for the formation of  
1235 secondary organic and inorganic aerosol. In all, the aerosol module consists of 16 tracers, which  
1236 are subject to processes such as hygroscopic growth, ageing, sedimentation.



IFS run ID	emissions	IFS version	IFS emission setup	IFS > 20 TROPOMI < 20			IFS < 20 TROPOMI > 20			IFS > 10 TROPOMI < 10			IFS < 10 TROPOMI > 10		
				N	mean ratio	median ratio	N	mean ratio	median ratio	N	mean ratio	median ratio	N	mean ratio	median ratio
BASE	GFASv1.4	CY47R3.1		60	8.65	7.66	2	2.94	2.94	260	5.46	4.28	45	2.74	2.56
BASE.CAP0.1	GFASv1.4	CY47R3.1	capped 0.1 mg m <sup>-2</sup> d <sup>-1</sup>	-	-	-	3	7.50	7.50	-	-	-	57	5.65	5.47
BASE.CAP0.3	GFASv1.4	CY47R3.1	capped 0.3 mg m <sup>-2</sup> d <sup>-1</sup>	2	3.30	3.30	3	4.14	4.21	19	3.05	2.48	56	3.68	3.51
GFA	GFA-S4F	CY47R3.1		497	14.24	11.10	2	3.16	3.16	1183	9.39	6.79	33	2.41	2.08
GFA.CAP0.3	GFA-S4F	CY47R3.1	capped 0.3 mg m <sup>-2</sup> d <sup>-1</sup>	9	8.02	5.71	3	4.36	4.61	87	4.88	3.94	55	3.36	3.13
GFA.IFSCYCLE	GFA-S4F	CY48R1.0		441	14.7	11.51	2	3.20	3.20	1034	9.66	7.07	37	2.40	2.22
BASE.BETA	GFASv1.4	CY48R1.0	β-optimized	27	12.15	11.96	2	1.58	1.58	67	7.23	4.58	37	2.35	1.97
GFA.BETA	GFA-S4F	CY48R1.0	β-optimized	51	23.17	17.09	2	1.42	1.42	122	13.06	7.39	36	2.33	1.90
GFA.SOIL	GFA-S4F	CY48R1.0	updated soil NO <sub>x</sub>	444	14.68	11.49	2	3.14	3.14	1072	9.54	7.00	37	2.34	2.18
GFA.BETA.SOIL	GFA-S4F	CY48R1.0	updated soil NO <sub>x</sub> β-optimized	99	24.87	15.08	1	1.62	1.62	258	14.02	7.84	22	1.33	1.82



1238 **Table A1.** Overview of IFS-COMPO-COMPO simulations used in this paper for the larger  
1239 Amazon region: four-letter/number IFS-COMPO simulation ID, fire emission database,  
1240 other emission specifics and IFS-COMPOIFS-COMPOversion. Right columns indicate the  
1241 IFS-COMPO simulation comparison with TROPOMI data statistics of the ratio between  
1242 simulated and observed daily tropospheric NO<sub>2</sub> columns for certain data selections.  
1243 Indicated are the number of IFS-COMPO grids meeting the selection criteria (N) and the  
1244 mean and median ratios. Data selections: IFS-COMPO > 20×10<sup>15</sup> molecules cm<sup>-2</sup> and  
1245 TROPOMI < 20×10<sup>15</sup> molecules cm<sup>-2</sup>; IFS-COMPO < 20×10<sup>15</sup> molecules cm<sup>-2</sup> and  
1246 TROPOMI > 20×10<sup>15</sup> molecules cm<sup>-2</sup> IFS-COMPO > 10×10<sup>15</sup> molecules cm<sup>-2</sup> and  
1247 TROPOMI < 10×10<sup>15</sup> molecules cm<sup>-2</sup>; IFS-COMPO < 10×10<sup>15</sup> molecules cm<sup>-2</sup> and  
1248 TROPOMI > 10×10<sup>15</sup> molecules cm<sup>-2</sup>

1249



	R <sup>2</sup> [PEARSON]	R <sup>2</sup> [SPEARMAN]	R <sup>2</sup> [PEARSON]	R <sup>2</sup> [SPEARMAN]
AMAZON				
	NO <sub>2</sub>		CO	
BASE vs BASE.BETA	0.925	0.900		
GFA vs GFA.BETA	0.774	0.757		
BASE vs GFA.BETA	0.631	0.556		
BASE vs GFA	0.709	0.586	0.680	0.539
BASE.BETA vs GFA.BETA	0.774	0.690		
GFA vs BASE.BETA	0.689	0.568		
BASE vs BASE.BETA				
AFRICA	0.978	0.976		
SIBERIA tundra	0.908	0.845		
SIBERIA steppe	0.249	0.309		

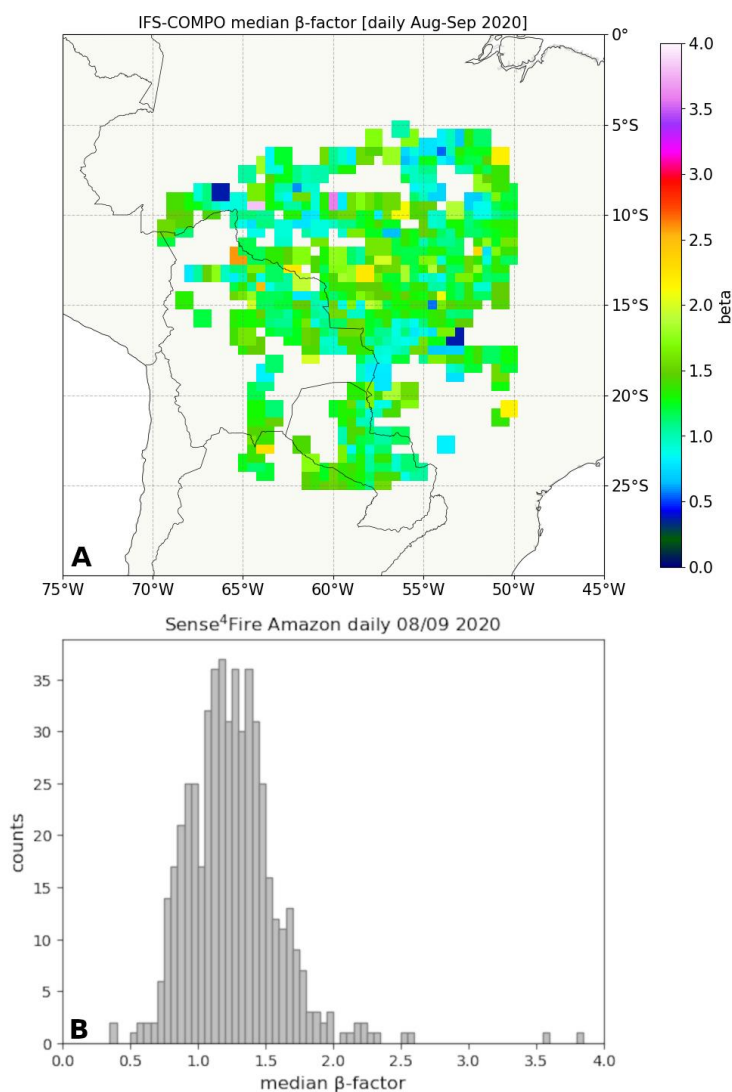
1250 **Table A2.** Spatial correlations of emissions databases used in this study for the four 20°×20°  
 1251 degree regions (Table 2). Note that the “BASE” simulation uses GFAS emissions. The lower  
 1252 three row contain the correlations for the non-Amazon regions for which only GFAS and β-  
 1253 optimized GFAS is available.



1254

1255 **Figure A1.** Location of the S4F test areas for the development of methods. Source: © Google

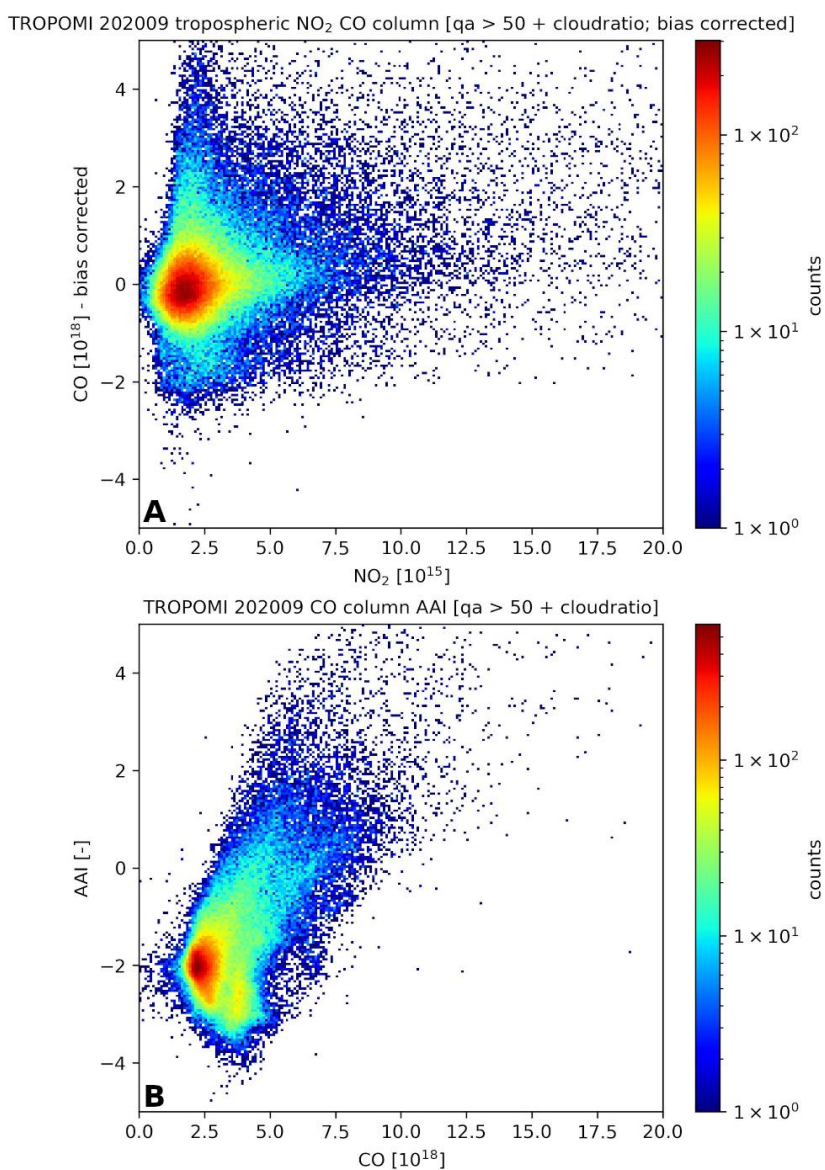
1256 Maps 2024, Satellite Basemap, global view, <https://www.google.com/maps/>, 26-03-2024



1257

1258 **Figure A2.** (A) Spatial distribution of IFS-COMPO values of the median  $\beta$ -factor over the  
1259 Amazon region based on: [1] daily simulation data for August-September 2020 [2] for model  
1260 grids with emissions larger than  $1 \cdot 10^{-10} \text{ kg m}^{-2} \text{ s}^{-1}$  and [3] model grid  $\text{NO}_2$  column values larger  
1261 than  $2 \times 10^{15} \text{ molecules cm}^{-2}$ . (B) Histogram of data displayed in panel (A).

1262

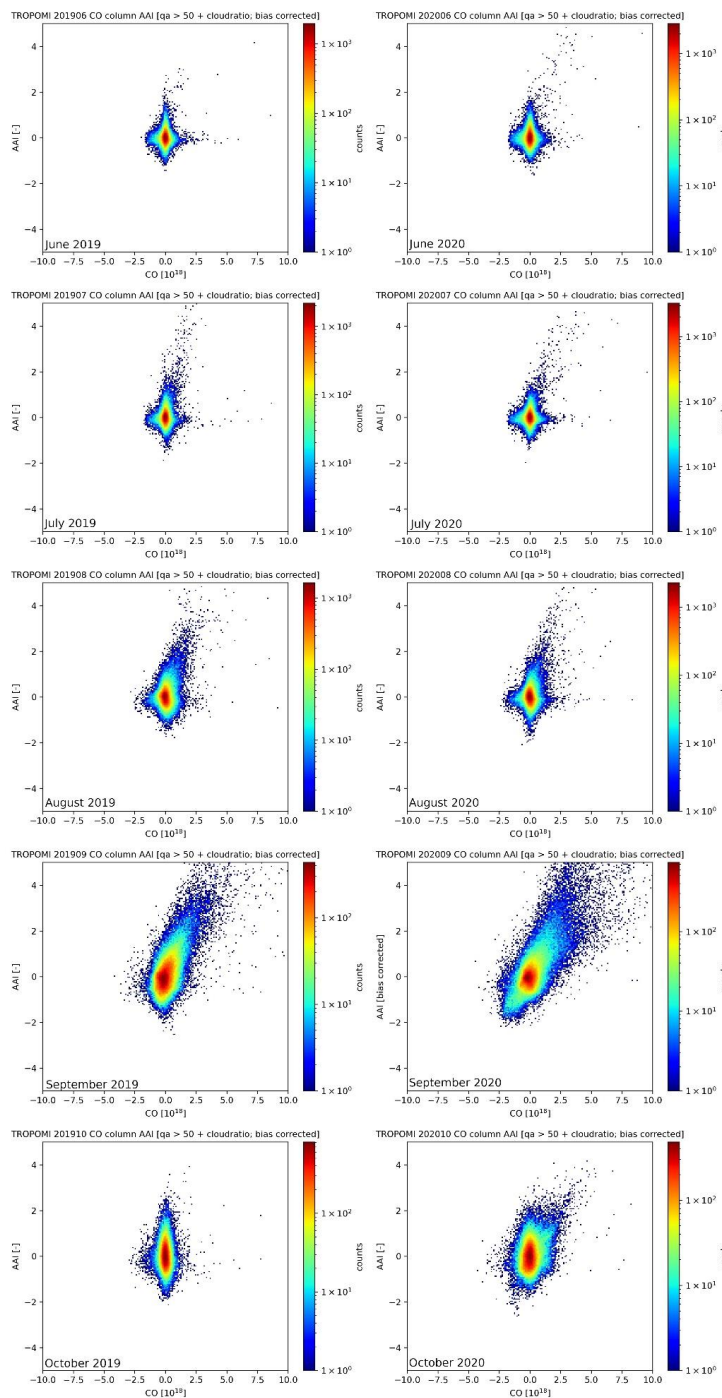


1263

1264 **Figure A3.** (A) As Fig. 3, upper panel but without applying a daily median value bias

1265 correction for both the TROPOMI daily AAI and CO data. (B) as Fig. 3, middle panel,, upper

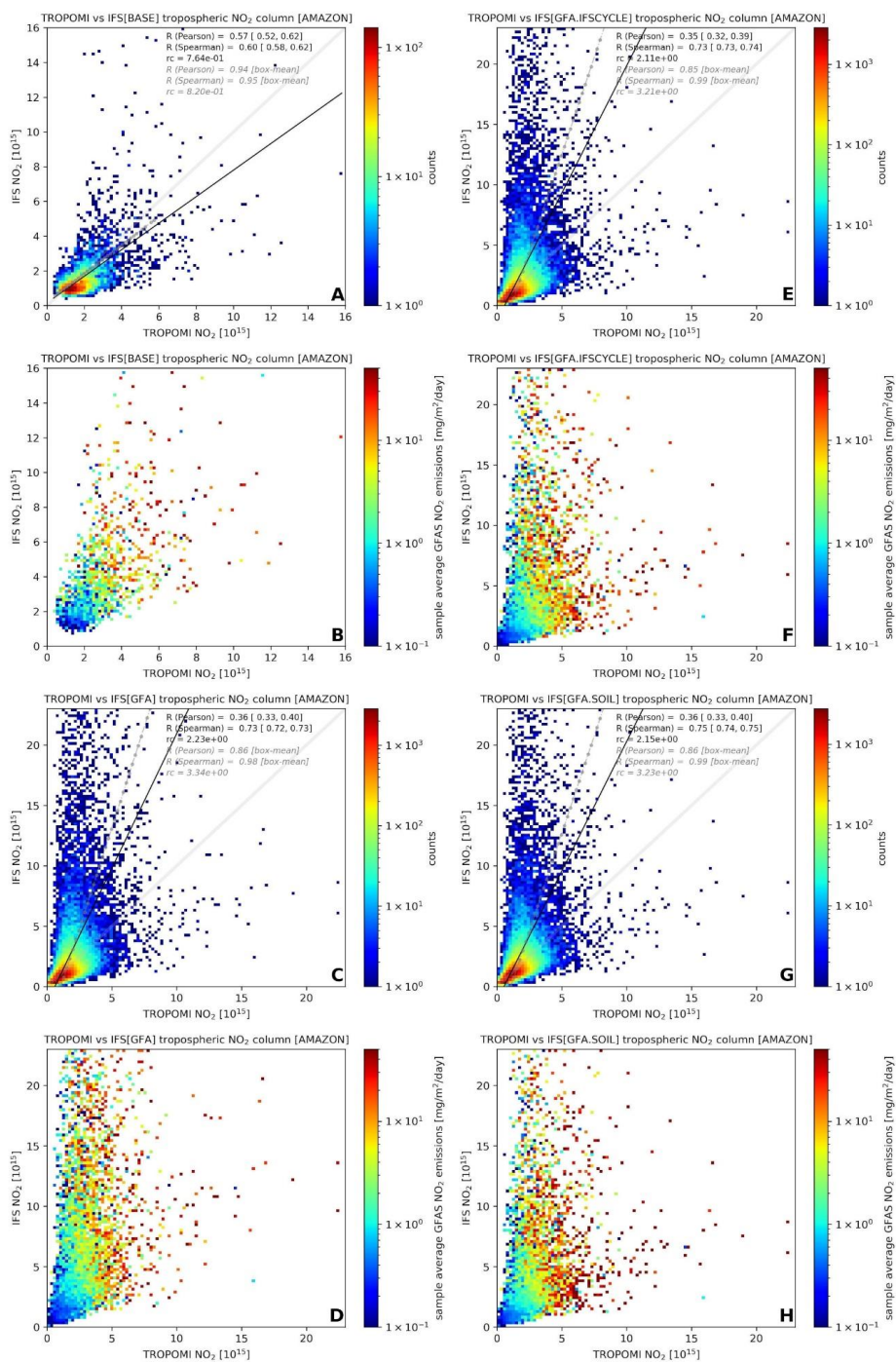
1266 panel but with applying a daily median value bias correction for TROPOMI CO data.







1268 **Figure A4.** As Fig. 3, upper panel (2D histogram of TROPOMI NO<sub>2</sub> tropospheric columns and  
1269 CO total columns, the latter bias corrected using the daily median CO total column value) but  
1270 for all individual months between June and October and for both 2019 and 2020.



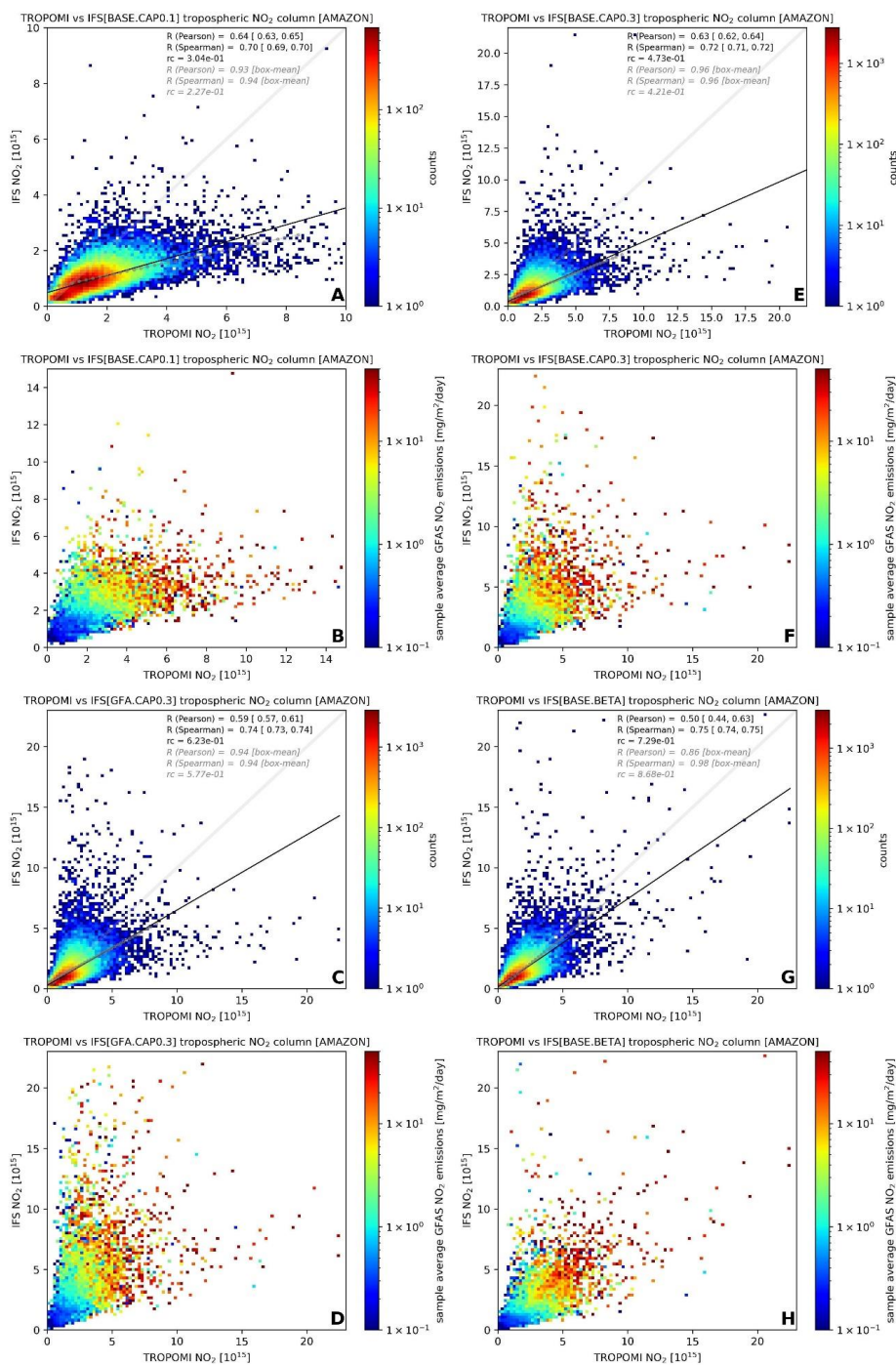
1271

1272



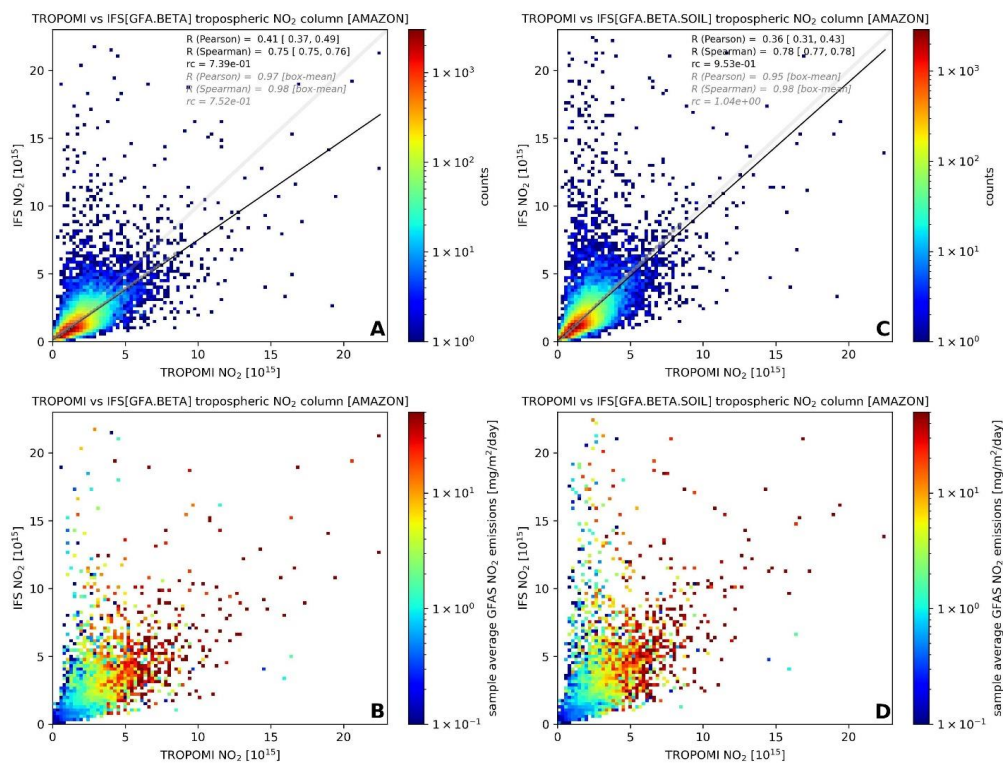
1273 **Figure A5.** As Fig. 5 but for (A, B) the smaller Amazon region as displayed in Figs. 1 and 2;  
1274 (C, D) as Fig. 5 but with GFA-S4F fire emissions; (E, F) as Fig. 5 but with GFA-S4F fire  
1275 emissions and for IFS-COMPO version CY48R1; (G, H) As Fig. 5 but with GFA-S4F  
1276 emissions over the Amazon region and with updated soil NO<sub>x</sub> emissions. Note that outside of  
1277 the Amazon (25°S-EQ, 85°W-30°W) GFAS emission are used instead of the GFA-S4F  
1278 emissions.

1279



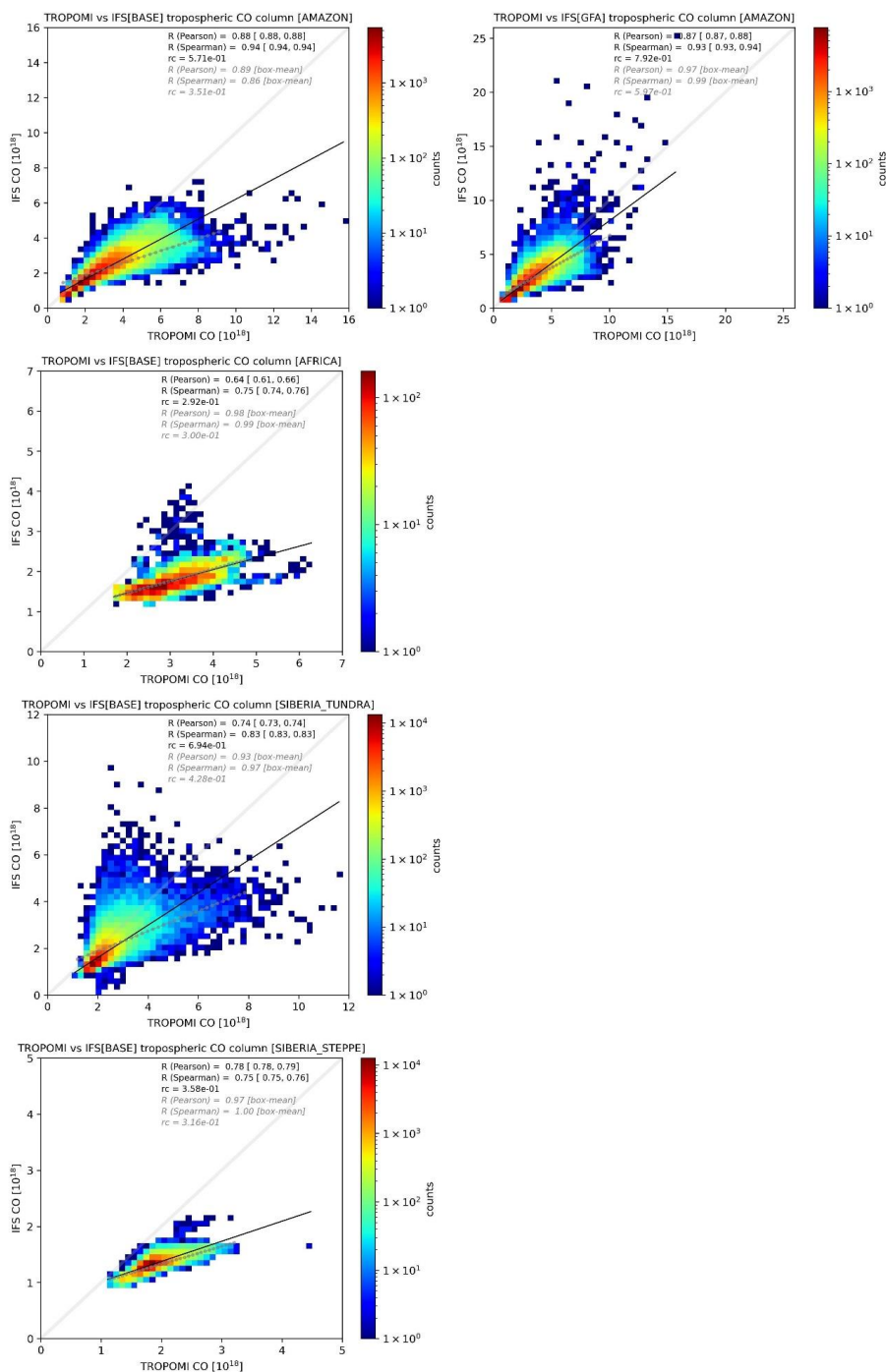


1281 **Figure A6.** As Fig. 5 but for (A, B) GFAS fire emissions capped at  $1 \cdot 10^{-10}$  kg m<sup>-2</sup> s<sup>-1</sup>; (C, D)  
1282 GFAS fire emissions capped at  $3 \cdot 10^{-10}$  kg m<sup>-2</sup> s<sup>-1</sup>; (E, F) GFA-S4F fire emissions capped at  
1283  $3 \cdot 10^{-10}$  kg m<sup>-2</sup> s<sup>-1</sup>; (G, H)  $\beta$ -optimized GFAS emissions.



1284

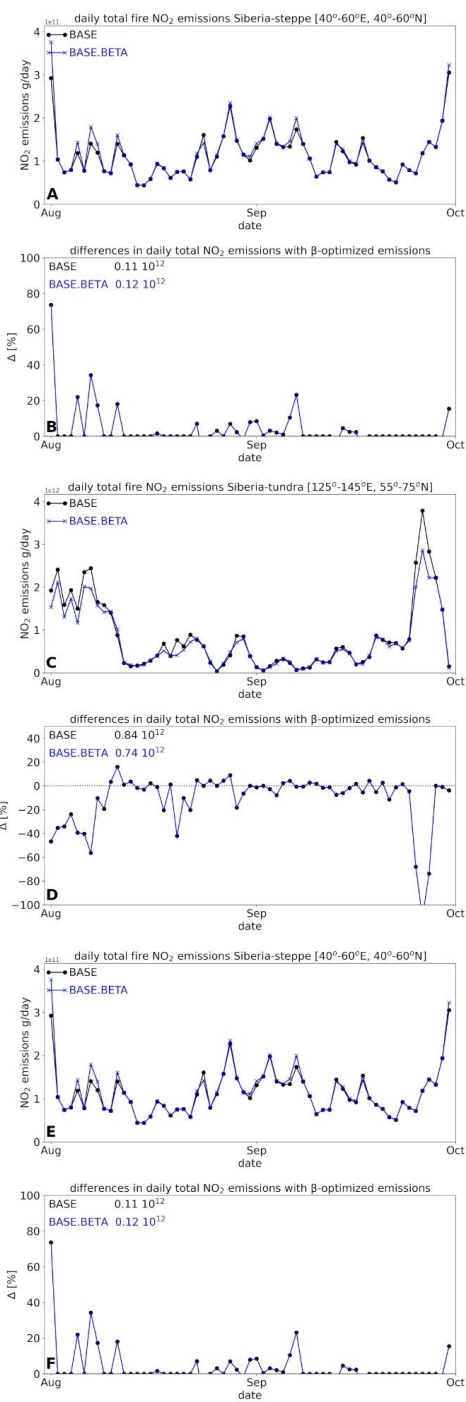
1285 **Figure A7.** As Fig. 5 (A, B) but for (A, B)  $\beta$ -optimized GFA-S4F emissions and (C, D)  $\beta$ -  
1286 optimized GFA-S4F emissions and with updated soil NO<sub>x</sub> emissions





1288 **Figure A8.** Comparison of IFS-COMPO and TROPOMI CO - similar to Figs. 6-7-8 but - for  
1289 four different regions based on GFAS emission (IFS-COMPO run BASE). For the Amazon  
1290 region also results from the IFS-COMPO simulation with GFA-S4F emissions are presented  
1291 (second panel; IFS-COMPO run GFA). Statistics are summarized in Table A2.





1292

1293





1294 **Figure A9.** Absolute and relative differences in regional daily NO<sub>x</sub> emissions as in Fig. 9 but  
1295 for (A, B) the sub-equatorial Africa region, (C, D) the Siberia tundra region and (E, F) the  
1296 Siberia steppe region. See Appendix Fig. A1 for the location of these regions.

1297